Structure and energetics of ZrC(100)||c-ZrO2(001) interface: A combination of experiments, finite temperature molecular dynamics, periodic DFT and atomistic thermodynamic modeling

Eric Osei-Agyemang, Jean-François Paul, Romain Lucas, Sylvie Foucaud, Sylvain Cristol, Anne-Sophie Mamede, Nicolas Nuns, Ahmed Addad

Structure and Energetics of ZrC(100)||*c*-ZrO_2(001) interface: A Combination of Experiments, Finite Temperature Molecular Dynamics, Periodic DFT and Atomistic Thermodynamic Modeling

Eric Osei-Agyemang[1], Jean-François Paul[2], Romain Lucas[3*], Sylvie Foucaud[3], Sylvain Cristol[2], Anne-Sophie Mamede[2], Nicolas Nuns[2], Ahmed Addad[4]

[1] Department of Materials Design and Innovation, University at Buffalo, Buffalo, New York 14260-1660, USA

[2] Univ. Lille, CNRS, Centrale Lille, Univ. Artois, UMR 8181 – UCCS – Unité de Catalyse et Chimie du Solide, Cité Scientifique, F-59655 Villeneuve d'Ascq, France

[3] Université de Limoges, IRCER, UMR 7315, F-87068 Limoges, France

[4] Univ. Lille, CNRS, INRAE, Centrale Lille, UMR 8207 - UMET - Unité Matériaux et Transformations, F-59000 Lille, France

Corresponding author: Dr. R. Lucas, IRCER-CNRS, UMR 7315
Centre Européen de la Céramique, 12 Rue Atlantis, F-87068 Limoges Cedex, France
Fax: (+)33587502304
E-mail: romain.lucas@unilim.fr

Abstract: The oxidation process of ZrC is very important as it affects its initial excellent mechanical and physical properties. ZrC is a ultra-high temperature ceramic, but forms low refractory oxides at lower temperatures of 500-600°C. To develop core/shell materials by coating the ZrC surface with another material that forms protective layers on ZrC and prevents it from oxidation (such as SiC), there is the need to study and characterize the oxidized layer surrounding ZrC particles. XPS, ToF-SIMS, TEM-ED and EDX analyses were used to study the covering oxidized layer, and polycrystalline ZrO_2(mainly cubic phase) was identified. Some traces of the tetragonal phase are observed to be present as shells around the ZrC particles with a thickness of about 4 nm on the average. Periodic DFT was subsequently used to characterize the interface formed between ZrC(100) and *c*-ZrO_2(001) phases. A strong interface was noticed mainly with charge transfer from Zr (c-ZrO_2 side) at the interface to O and C (ZrC side) atoms at the interface. The interfacial properties are local to only the first and second layers of ZrO_2, and not on the third and fourth layers of ZrO_2, as Bader charge analysis revealed substantial charge transfer at the interface region with no charge redistribution in the second ZrO_2 layer and subsequent bulk layers. The main physical quantity, ideal work of adhesion (W_{ad}), used to characterize the interface, remains quite constant for all ZrO_2 layers, and converges at three layers of ZrO_2. The interfacial bonds formed are observed to be stronger than the free surfaces in the corresponding ZrC and *c*-ZrO_2 used to generate the interface.

1. Introduction

One important Transition Metal Carbide (TMC) known for its excellent physico-chemical and structural properties is zirconium carbide (ZrC). Being an Ultra High Temperature Ceramic (UHTC) with an extremely high melting point of 3430 °C, it is used in applications involving harsh conditions such as coatings of the inside walls of nuclear plants, hard materials like cutting tools and in the aerospace industries as nozzle flaps. [1,2]

Despite its excellent mechanical and physical properties, its use in extreme corrosive and oxidizing environments is limited. Indeed, ZrC forms low refractory oxides at temperatures of around 500-600 °C. [6]

To understand this phenomenon, several studies have been carried out on the different oxidation processes on the ZrC model surfaces. ZrC belongs to the Fm3m space group. It is a face centered cubic crystal and crystallizes in an NaCl crystal structure type. [3] It has three distinguishable low index surfaces with stabilities in the order of (100) > (111) > (110). [4,5] A considerable amount of research has been carried out on the oxidation of ZrC(111) surface, both experimental and theoretical. [7-10] All these studies have shown very strong interactions of oxygen with ZrC(111) surface. Oxygen is found to adsorb dissociatively as atomic oxygen and sits at three-fold hollow fcc sites between three surface Zr atoms. This adsorption process is found to be accompanied by extremely high reaction energies.

In an experimental study on the oxidation of ZrC single crystals, they were oxidized isothermally at temperatures of 600-1500 °C in a mixed atmosphere of O_2, also with O_2 partial pressures of 0.02-2 kPa for 1-20 hours. Preferred orientation of tetragonal or monoclinic ZrO_2 were occasionally observed on ZrC surfaces. [11] The authors further analyzed XRD patterns on the crystal oxidized at 600 °C for one hour with a pressure of oxygen P_{O2} = 2 kPa. It showed the presence of cubic ZrO_2 together with the substrate ZrC. Subsequent XRD analysis indicated a preferred (110) or (200) orientation of *t*-ZrO_2 or a preferred (200) or (220) orientation of *m*-ZrO_2, for the oxidation of the (200) or (220) planes of a ZrC crystal, respectively. In another work, a crystallographic relationship such as the (200) and (220) planes of ZrC being parallel to the (200) and (220) *c*-ZrO_2 was established at the ZrC/ZrO_2 interface. [12]

Even though there is not much work neither experimental and theoretical, describing the oxidation process on the ZrC (110) surface, in a recent paper, a complete discussion on the oxygen adsorption process and mechanism of oxidation was provided. [13] The (110) surface was observed to adsorb oxygen dissociatively and led to a subsequent formation of a layer of ZrO_2 on the surface, with the release of CO_2 into the gas phase. This work complements the other oxidation studies performed on the ZrC(100) and (111) surfaces. [4, 7-10, 14-18]

Several studies have also been reported on the adsorption and oxidation of ZrC(100) surfaces. Different accounts on a variety of oxidation processes were reported for the ZrC(100) surface. [14-18] Theoretical studies have shown dissociative adsorption of oxygen into atomic species sitting at mmc sites (between two surface Zr atoms and one carbon atom). [16,18,19] In some of these reports, not only did the mode of oxygen adsorption alone studied, but also the mechanism for subsequent exchange of adsorbed O atoms and surface C atoms with final removal of CO.

[16,17,19] In another report, the oxidation of ZrC(100) surface led to the formation of a ZrO-like layer in the form of ZrO_x ($1 < x < 2$). [15] Details of the electronic structure of this oxidized layer (ZrO-like layer) were also reported in another paper. [20] In a separate work, oxidation of the ZrC(100) surface led to the formation of *c*-ZrO_2 (200) on the ZrC facets. [12]

In light of the above stated observations on the formation of ZrO_2 on the ZrC surfaces, it was necessary to study the structure, stability and energetics of the ZrC(100)/*c*-ZrO_2 interface. Indeed, the control of the surface chemistry of ZrC would lead to a better understanding of the reactivity of it, to enable the functionalization with organic molecules and more particularly SiC preceramic precursors (*e.g.* polycarbosilanes). It will lead to hybrid materials with high performance properties (*i.e.* better resistance to oxidation). [4,13,18] To answer this need, this paper is organized as follows: section 2 describes experimental conditions and setup for analyzing the ZrC particles and the theories, methods and procedures used in this study. In section 3.1, the results of the experiments will be discussed, while section 3.2 will concentrate on the results from molecular dynamics simulation of ZrO_2 growth on the ZrC(100) surface. Section 3.3 to 3.5 will focus on the bulk, surface, interfacial strength, thermodynamic and electronic properties at the interface. Eventually, section 4 will provide summary and conclusions on the current work.

2. Experimental

2.1 XPS, ToF-SIMS and TEM-ED Experimental Analysis

A combination of XPS, ToF-SIMS and TEM-ED experiments were performed on the ZrC nanocrystallites to determine the nature and content of the oxidized layer. All the analysis were performed on the technological of the Chevreul Institute in Lille.

The XPS analyses were performed using a Kratos Analytical AXIS Ultra^{DLD} spectrometer. A monochromatic aluminium source (Al Kα = 1486.6 eV) was used for excitation. The analyzer was operated in constant pass energy of 40 eV using an analysis area of approximately 700 µm x 300 µm. Charge compensation was applied to compensate for the charging effect occurring during the analysis. The ZrO_2 phase O 1s (530.0 eV) binding energy (BE) was used as internal reference. Quantification and simulation of the experimental photopeaks were carried out using CasaXPS software. Quantification considered a non-linear Shirley background subtraction. [21]

ToF-SIMS analyses were performed on a TOF.SIMS^5 instrument (IONTOF GmbH, Münster, Germany) equipped with a 25keV bismuth primary ion source. Charging effect due to the primary ion beam was compensated with pulsed low energy electrons (20 eV). Static acquisitions were performed in both polarity with Bi_3^+ primary ions. Prior to analysis, the powder was tableted to obtain a better mass resolution and secondary ion yield. Negative and positive ToF-SIMS spectra were compared with a reference of ZrO_2. Dual beam mode was used for depth profiling. For dynamic SIMS Cs^+ (0.5kV and 1kV) were used for sputtering in the non-interlaced mode to obtain better depth resolution on the ZrC to characterize the thin ZrO_2 surface layer.

An FEI Tecnai G2 microscope, operating at 200 kV was used for the TEM-ED experiments performed on the ZrC particles to obtain the crystalline nature. A dry powder deposition on Cu grid with carbon film was used.

2.2 Calculation Scheme and Structural Models

2.2.1 General Interface Computational Details

All parameters used for the interface calculations are based on optimized parameters for the ZrC substrate.

We performed all theoretical calculations with the Vienna ab initio Simulation Package (VASP) [22] which is based on Mermin's finite temperature DFT. [23] For the Zr, O, H and C atoms, the electronic configurations used are $[Kr]4d^2 5s^2$, $[He]2s^2 2p^4$, $1s^1$ and $[He]2s^2 2p^2$, respectively. The Projected Augmented Wavefunction (PAW) pseudo-potentials [24] were used for representing the core electrons and the core part of the valence electrons wavefunctions. For the exchange correlation functional, the generalized gradient approximation (GGA) parameterized by Perdew, Burke and Ernzerhof (PBE) [25] was used and the Methfessel-Paxton, [26] smearing scheme was utilized by setting the gamma parameter to 0.1 eV. An optimized energy cut-off of 500 eV was used for the plane wave basis set in describing the valence electrons while the integration of the Brillouin zone was performed with a standard Monkhorst-Pack [27] special grid of 9 x 9 x 9 k-points for the bulk and 9 x 9 x 1 k-points for surface and interface calculations. The self-consistent field (SCF) procedure for resolution of the Kohn-Sham equations was assumed to be converged when energy changes of 1×10^{-4} eV between two successive iterations are reached.

2.2.2 Finite Temperature Molecular Dynamics

We performed finite temperature molecular dynamics to confirm the ZrO_2 phase formed on ZrC surfaces as evidenced by XPS, TOF-SIMS and TEM-ED experiments. A (2 x 2) supercell was used for all MD simulations. This simulation was started with a thick layer of ZrC (100) surface slab while enough Zr and O atoms were deposited on the exposed ZrC surface to form about two layers of ZrO_2. Within the micro canonical ensemble, the ions were initially kept at T = 100 K and the velocities scaled upwards at different steps until a final temperature of 1000 K was reached. This temperature was selected to allow for the possibility of forming of the *m*-ZrO_2 phase which is stable at low temperatures below 1450 K. A time step of 1 fs was used. The resulting equilibrium structure was then quenched from 1000 K to 500 K and the final resulting structure was optimized with the previous parameters.

2.2.3 Bulk Phases of ZrC and ZrO_2

To facilitate discussions of the electronic and mechanical properties of the interfacial structure model used, a brief discussion of the major characteristics of bulk electronic structure of ZrC and ZrO_2 is provided.

Cubic ZrC belongs to the *Fm3m* space group, crystallizes in an fcc structure, and has two special atomic positions for Zr and C at (0 0 0) and (0.5 0.5 0.5) respectively as shown in figure 1. It has an experimental lattice parameter of 4.696 Å. [28] Details on calculation of optimized bulk parameters are found elsewhere. [18] In optimizing the geometrical structure, the positions of all ions were relaxed until the forces beeing smaller than 1 x 10^{-2} eV/Å. The lattice parameter for the ZrC bulk was optimized by fitting the energy versus volume curve with the Murnaghan's equation of state as detailed in our previous work. [28] Thus the optimized lattice parameter was calculated as 4.736 Å and the difference with the experimental one is lower than 1%, typical of GGA functional calculations. [18] All ZrC and ZrO_2 bulk calculations involved cells with 4 formula units (Figure 1).

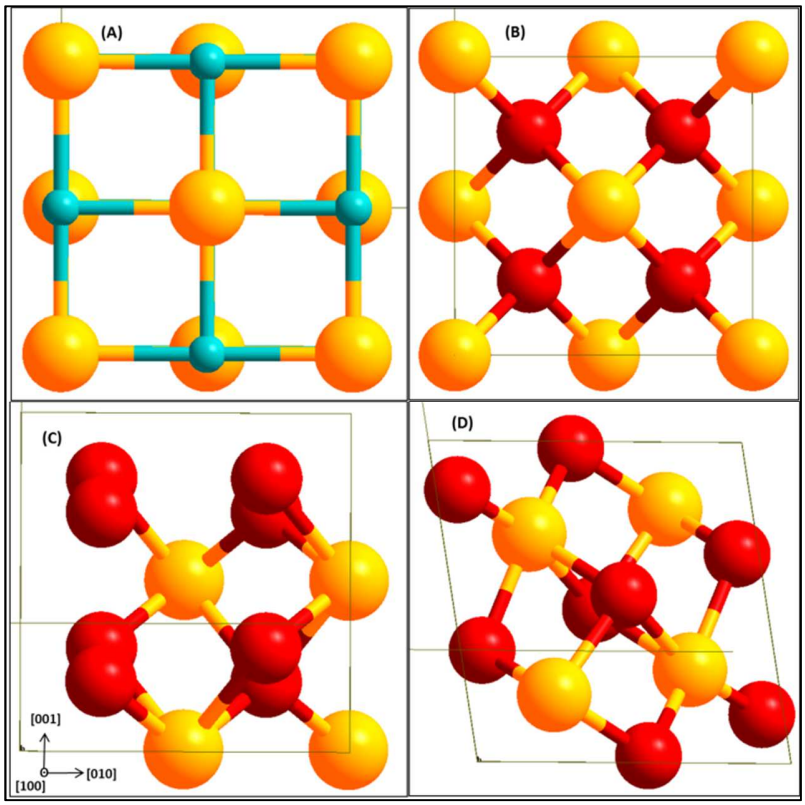

Figure 1. Bulk structures of ZrC(A), *c*-ZrO_2(B), *t*-ZrO_2(C) and *m*-ZrO_2(D). Yellow(Zr), light blue(C) and red(O)

The *c*-ZrO_2 has a $Fm\bar{3}m$ crystal structure. Starting from the experimental crystallographic positions, the volume of the cell was decreased and increased by about 20% and the resulting total energy calculated. The pairwise calculated values of volume and energy were fitted using the Murnaghan's equation of state.

The tetragonal ZrO_2 (*t*-ZrO_2) has the tetragonal symmetry $P4_2/nmc$ and only differs from the cubic phase in the small alternating distortion of the O atom columns along the 4_2 axes in the [001] direction. Compared to the *c*-ZrO_2, there is also a small elongation of the *c* lattice parameter along the [001] direction. Since optimizing the *c*-ZrO_2 structure along the c axis results in a distortion of the O atoms in the perpendicular direction, and subsequently yielding a tetragonal structure, lattice parameters for *t*-ZrO_2 were calculated as well. Optimization of the

lattice parameter was started from the experimental cell with *a* = 3.596 Å and *c* = 5.187 Å [29] and the energy versus volume data fitted with the Murnaghan's equation of state.

The monoclinic ZrO_2, *m*-ZrO_2 belongs to the space group *P21/c.* This phase is also defined by another parameter, the angle β with an experimental value of 99.23°. Starting from experimental lattice parameters determined by Yashima et.al, [30] energies were calculated at different volumes and fitted the data with the Murnaghan's equation of state.

2.2.4 Construction of Interface Model

In developing an interface from two different bulk phases, a step-by-step approach is taken. An initial determination of the stacking direction at the interface needs to be selected, and from this identified interface plane, the two different bulk phases should have a proper commensurability factor. [31] The two bulk phases are then cleaved to reveal the selected surfaces for the interfacial structure. These surfaces will have different terminations of different atomic layers. The two surfaces are then brought together in contact with each other to form the interfacial structure which is then fully relaxed to obtain the final optimized configuration at the interface.

2.2.4.1 Surface structures and commensurate phases

The different low index surfaces of ZrC have been extensively studied. The (100) surface is found to be the most stable, being stoichiometric and non-polar. [4,5,18] With its lattice parameter of 4.736 Å, this surface has an exposed surface area of 22.468 $Å^2$. The ZrC(100) bulk phase is used as the substrate onto which the ZrO_2 is grown. Different studies have been made on the stability of the different surfaces of *c*-ZrO_2. [32,33] The *c*-ZrO_2 (111) surface is the most stable followed by the (110) and then the (100) surface for both relaxed and unrelaxed surfaces. In this work, the surface energies for 1 layer up to 6-layers of ZrC were calculated. The surface energies were obtained with the expression $E_{surf} = (1/2A)\ [\ E_{slab} - nE_{bulk}\ ]$ where E_{slab} is the total energy of the surface slab, E_{bulk} is the energy per formula unit of ZrC or ZrO_2 in the corresponding bulk, *A* is the surface area and *n* is the number of formula units in the surface slab.

Surface energies were also calculated for the (001) terminations of *c*-ZrO_2, *t*-ZrO_2 and *m*-ZrO_2. The surface energies were obtained for different layers of ZrO_2 starting from 1 layer up to 6 layers of ZrO_2. Indeed, these surface energies are needed to calculate the interface tension defined in section 2.4.3.

The *c*-ZrO_2 (001) surface can have different sequence of layering at the terminated surface. As can be seen in figure 1, it can be considered terminating as Zr|OO|Zr|OO|Zr|OO….. and, in this case, half of the oxygen atoms are located behind the front oxygen atoms on the same plane. The termination can be flipped to get another one. Another termination that can be built is the O|Zr|OO|Zr|OO|Zr|O…. termination. With this configuration, oxygen layers terminate both exposed surfaces. Thus three different surface terminations can be used for building an

interface with the ZrC(100) surface. A Zr-terminated, O-terminated or OO-terminated surface of *c*-ZrO_2 (001) can be used for the interface structure.

A problem that arises in interfacial studies was the fact of making two different phases commensurate with each other. This interface coherence requirement is due to the periodic boundary conditions used in the calculations at the interface and to the periodic nature of the crystal. Thus, a unit cell for the interface structure must be selected. One geometrical principal measure used in ensuring this commensurability is the surface mismatch parameter ϒ. [34] With this measure, a surface unit cell of *c*-ZrO_2 with an area S_2 is coherently forced onto a substrate ZrC (100) surface with a surface unit cell of area S_1 (Figure 2). The mismatch parameter is then calculated as:

$$\Upsilon = 1 - \frac{2S_{1-2}}{S_1 + S_2} \ldots\ldots\ldots eq.(1)$$

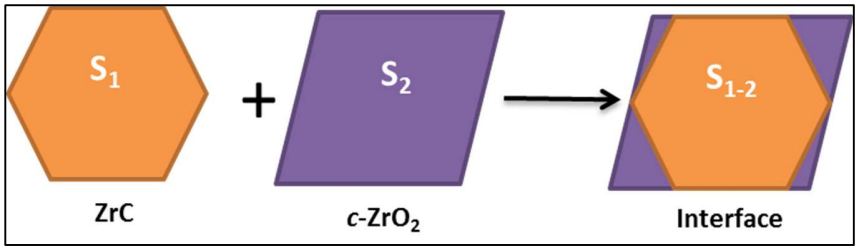

Figure 2. Scheme of the interface between a substrate unit cell of *c*-ZrO_2 with a ZrC(100) surface, leading to the overlapping area

S_{1-2} is the overlapping area between the two commensurate surfaces (Figure 1). This misfit parameter does not measure an area mismatch but rather an average length scale misfit between the two unit cells. [35] Table 1 shows the calculated mismatch parameters for the different *c*-ZrO_2 surfaces on ZrC(100) surface using a ZrC lattice parameter of 4.736 Å and a *c*-ZrO_2 lattice parameter of 5.143 Å. It is obvious that the lattice mismatch for all *c*-ZrO_2 surfaces on the ZrC(100) surface is less than 40%. Thus from this table, it suddenly becomes apparent that the ZrC(100)||*c*-ZrO_2(001) interface combination with a misfit parameter ϒ of 8.2% is the best choice. This interface unit cell that is defined by the substrate ZrC(100) phase is cubic, small, with a surface of 4.736 Å x 4.736 Å, and can be easily managed.

Table 1. Surface mismatch parameter ϒ calculated for different combinations of ZrC and *c*-ZrO_2 surface

ZrC	*c*-ZrO_2	Overlap area(S_{1-2})/Å^2	Misfit (ϒ)
(100)	(001)	22.434	0.082
(100)	(110)	22.434	0.250

(100)	(111)	22.400	0.279

This mismatch parameter which is a geometrical measure cannot be used alone in building the interface structure. Other models and factors need to be considered. Two different methods for ensuring commensurability of two different phases can be found in the literature. In the first approach, sufficiently large unit cells of both phases are used. Thus, the basic unit cells of each of the two different phases are increased in size in a subsequent manner until the two phases are commensurate with each other. This approach leads to interfacial structures with very small mismatch parameters and still some incoherent areas at the interface. [36] The interface models formed in this approach are however too huge and not suitable for ab initio methods.

In the second approach that is used in many interfaces' calculation studies, [37-42] a single unit cell is used at the interface plane, and it is generally termed as the (1 x 1) model. One phase is considered as the substrate, and its lattice parameters are used. The lattice parameters of the other phase are scaled until a perfect matching of the two lattice phases is obtained. This method is suitable for interface models with very little mismatch parameters, and we decided to adopt this approach for the current study.

2.2.4.2 Interface Model Geometry

A slab geometry model was used to study the interfacial structure and its properties. The ZrC phase was selected as the substrate with a thickness of 10.945 Å, which corresponds to 9 layers of ZrC. The selected substrate thickness was considered enough to form the required interfaces and mimic the electronic structure with ionic relaxations in the bulk ceramic. [33] The *c*-ZrO_2 units were then pinned onto the ZrC (100) exposed surface, layer by layer. Coherent interfaces were thus ensured by straining the *c*-ZrO_2 (001) units to match the dimensions of the ZrC(100) surface. The bulk parameter and surface area of the ZrC (100) unit cell defines the interface structure model unit cell. In doing so, the *c*-ZrO_2 (001) unit cell lattice parameter is shrunk by about 8.6% relative to the equilibrium lattice of 5.143 Å. In fixing the orientation of the geometries of the two lattices at the interface, the remaining degrees of freedom in the final interface geometry after optimization is the perpendicular direction to the interface as well as the chemical composition of the interface. [43] Up to 5 layers of the *c*-ZrO_2 (001) units were built on the ZrC(100) surface.

Figure 3 shows side views of the different interface models used. Each *c*-ZrO_2 bilayer unit is approximately 3.5 Å thick. We ensured that all the models used are symmetric with respect to the center of the interface structure. This is done to ensure no long-range dipole-dipole interaction between exposed surfaces of the interface slab. Thus, each interface slab contains two identical interfaces. A vacuum of more than 13 Å was applied between two subsequent interface slabs to avoid any physical interactions between the slabs. Thus the interface slab configuration has a sequence of ---*c*-ZrO_2(001)||ZrC(100)||*c*-ZrO_2(001)|vacuum|*c*-ZrO_2(001)||ZrC(100)||*c*-ZrO_2(001)|vacuum| *c*-ZrO_2(001)||ZrC(100)||*c*-ZrO_2(001)|vacuum| *c*-ZrO_2(001) ---

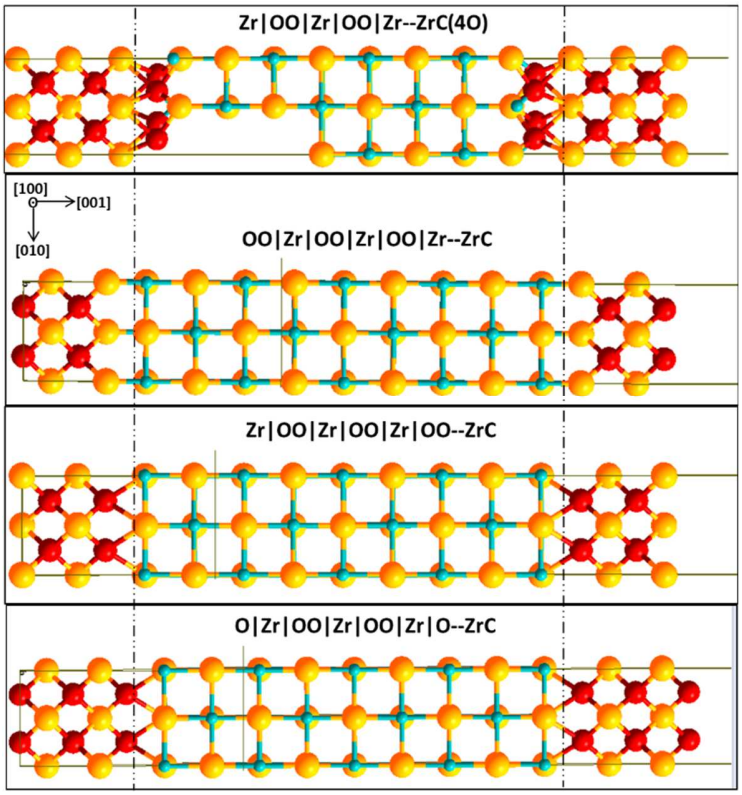

Figure 3. Interface structure models. Vertical dashed lines pass through bonds formed at the interface. Yellow(Zr), light blue(C), red(O)

The ZrC(100) surface has a single layer terminating with the same number of Zr and C atoms. This surface is very compact and hence the interface chemical composition is defined by the terminating layer of the *c*-ZrO_2(001) phase. Along the [001] direction of bulk *c*-ZrO_2, three different terminations, Zr|OO|Zr|OO|Zr|OO-, O|Zr|OO|Zr|OO|Zr|O-, OO|Zr|OO|Zr|OO|Zr- and hence three different interface models can be built from these as shown in figure 3. Moreover, in a previous study, [13] the oxidation of ZrC(100) surface led to the adsorption of 4 oxygen atoms on the surface, resulting in a full layer coverage. The synthesis of ZrC is mostly carried out in an oxidizing environment. It is therefore necessary to build another model with an oxidized ZrC(100) surface. Thus the fourth interface model consists of *c*-ZrO_2(001) terminating on both sides with Zr atoms on an oxidized ZrC(100) surface as shown in figure 3.

2.2.4.3 Interface Cohesion and Mechanics

An important parameter used in defining interface cohesion and stability is the interface tension γ_{int}, defined as the reversible work needed to separate the interface into two free surfaces. [44] With this definition, both plastic and diffusional degrees of freedom are assumed to be suppressed and hence negligible. From this definition, the greater the γ_{int} value, the higher the energy needed to separate the two surfaces at the interface.

According to Dupre equation, the interface tension can be defined in terms of the interface and free surface energies as: [45,46]

$$\gamma_{int} = \sigma_{ZrC} + \sigma_{c-ZrO_2} - \sigma_{ZrC||c-ZrO_2} \ldots\ldots eq.(2)$$

σ_{ZrC} and σ_{c-ZrO_2} are the relaxed surface energies of the ZrC and *c*-ZrO_2 surfaces respectively while $\sigma_{ZrC|c-ZrO_2}$ is the interface energy which is also defined as the adiabatic work of adhesion, $W_{ad} > 0$. Thus the relative strength of the interface versus the bulk bonds decides the preference for the interface formation or the open surfaces.[47] The adiabatic work of adhesion is defined as:

$$W_{ad} = \frac{E^{tot}_{ZrC} + E^{tot}_{c-ZrO_2} - E^{tot}_{ZrC||c-ZrO_2}}{2A} \ldots . eq.(3)$$

Where $E^{tot}_{ZrC}\ and\ E^{tot}_{c-ZrO_2}$ refer to the total energies of the full relaxed isolated ZrC and *c*-ZrO_2 slabs. The energy of the *c*-ZrO_2 slabs is computed taking into account the stress to fit the ZrC crystal parameter . $E^{tot}_{ZrC||c-ZrO_2}$ is the total energy of the fully relaxed interface slab and A is the interface area. The calculated W_{ad} value is usually a lower bound of values obtained by cleavage experiments due to dissipative processes in physically separating the interface.[44] Characterization of the interfacial strength is unrelated to the bulk strain in the deposited *c*-ZrO_2 and hence the $E^{tot}_{c-ZrO_2}$ value used is the total energy of the strained *c*-ZrO_2 in order to commensurate with the ZrC surface. Thus, the strain energy component is cancelled between $E^{tot}_{c-ZrO_2}$ and $E^{tot}_{ZrC||c-ZrO_2}$ since the *c*-ZrO_2 is in the strained state. [47]

Another important parameter is the rigid work of adhesion, W^{rigid}_{ad} which provides maximum cancellation of the strain energy from the interface energy obtained. [43] This can be achieved by ensuring the same strain state exists in both the free surfaces and the interface. This quantity is very useful in comparing the stability of the various interfaces with respect to cleaving from the two different phases. This quantity is the only measure which holds information purely on the bonding at the interface irrespective of the free surfaces. [43] W^{rigid}_{ad} is calculated by rigidly cleaving the relaxed interface structure to produce the free surfaces and not allowing the free surfaces to fully relax.

The interface tension can be used to provide a measure of whether the interface formation or the formation of the free individual surfaces are preferred. The sign and magnitude of γ_{int} in equation 2 also provides a measure for whether the interface bonds are stronger than the internal bonds in each separate phase. [47] In this case, $0 < \gamma_{int} < \sigma_{ZrC} + \sigma_{c-ZrO_2}$ corresponds to weakly coupled interface and $\gamma_{int} < 0$ to strongly coupled interfaces. The calculated values of $\sigma_{ZrC}\ and\ \sigma_{c-ZrO_2}$ are obtained from their respective relaxed equilibrium bulk phases (strain free *c*-ZrO_2 (001) surface).

2.2.5 Interfacial Thermodynamic Stability

An assessment of the thermodynamic stabilities of the different interface models was carried out. In this manner, the thermodynamic stability of the three different models of *c*-ZrO_2 on ZrC was assessed using the excess interface grand potential, $\Omega_{int}^{i/j}$ of an overlayer *j* on a substrate *i*, with respect to the ZrC and *c*-ZrO_2 bulks as reference instead of the surface slabs without constraints. The excess interface grand potential was calculated as follows:

$$\Omega_{int}^{i/j} = \frac{1}{2}\left[\Omega_{slab}^{i/j} - N_{ZrC}\Omega_{ZrC} - N_{ZrO_2}\Omega_{ZrO_2}\right] - \Omega_{ZrO_2}^{surf} \ldots . eq.(4)$$

$\Omega_{ZrO_2}^{surf}$ is the surface grand potential of the exposed ZrO_2 side of the interface slab which is in contact with the external environment. Assuming no temperature and pressure contributions to the grand potentials, the remaining bulk grand potentials can be defined as:

$$\begin{cases} \Omega_{slab}^{i/j} = E_{slab}^{i/j} - \sum_k N_k\mu_k \\ \Omega_{ZrC} = E_{ZrC}^{bulk} - \mu_{ZrC} \\ \Omega_{ZrO_2} = E_{ZrO_2}^{bulk} - \mu_{ZrO_2} \end{cases} \ldots\ldots eq.(5)$$

N is the number of each chemical species in the slab and μ is the corresponding chemical potential of that species. $E_{ZrC}^{bulk}\ and\ E_{ZrO_2}^{bulk}$ are the total bulk energies of ZrC and ZrO_2, respectively. When the systems are in thermodynamic equilibrium, the chemical potentials of ZrC and ZrO_2 can be written as: $\mu_{ZrC} = \mu_{Zr} + \mu_C\ and\ \mu_{ZrO_2} = \mu_{Zr} + 2\mu_O$. Substituting these relations with equation 5 into equation 4 with further rearrangements, we obtain the following equation:

$$\Omega_{int}^{i/j} = \frac{1}{2}\Big[E_{slab}^{i/j} - N_C E_{ZrC}^{bulk} - N_{ZrO_2}E_{ZrO_2}^{bulk} - \mu_{Zr}\big(N_{Zr} - N_C - N_{ZrO_2}\big) - \mu_O\big(N_O - 2N_{ZrO_2}\big)\Big] - \Omega_{surf}^{ZrO_2} \ldots\ldots\ldots eq.(6)$$

If we define a change in chemical potential related to the reference stable bulk Zr ($\Delta\mu_{Zr} = \mu_{Zr} - \mu_{Zr}^*$ with $\mu_{Zr}^* = E_{Zr}^{bulk}$) and O_2 gas ($\Delta\mu_O = \mu_O - (E_{O_2}^{Gas}/2)$) and substitute these in equation 6, we obtain the following equation:

$$\gamma_{int}^{i/j} = \frac{\Omega_{int}^{i/j}}{A} = \emptyset_{int}^{i/j} + \frac{1}{2A}\left[\Delta\mu_{Zr}\big(N_C + N_{ZrO_2} - N_{Zr}\big) + \Delta\mu_O\big(2N_{ZrO_2} - N_O\big]\right. \ldots eq.(7)$$

Where the interface dependent term $\emptyset_{int}^{i/j}$ is defined as:

$$\emptyset_{int}^{i/j} = \frac{1}{2A}\left[E_{slab}^{i/j} - N_{ZrC}E_{ZrC}^{bulk} - N_{ZrO_2}E_{ZrO_2}^{bulk} - E_{Zr}^{bulk}\left(N_{Zr} - N_C - N_{ZrO_2}\right) - \frac{E_{O_2}^{Gas}}{2}\left(N_O - 2N_{ZrO_2}\right)\right] - \gamma_{ZrO_2}^{surf} \ldots eq.(8)$$

$\gamma_{ZrO_2}^{surf}$ is the surface energy of the exposed ZrO_2 surface to vacuum. The interface grand potential is dependent on the chemical potential of oxygen and zirconium. The upper limit of the chemical potentials is defined with respect to the total energy of bulk Zr and molecular O_2 while the lower limit is with respect to the formation energy of ZrO_2. The limits are defined in equations 9 and 10 as:

$$\begin{cases} \Delta\mu_O = \mu_O - \dfrac{E_{O_2}^{Gas}}{2} < 0 \\ \Delta\mu_O > \dfrac{E_{ZrO_2}^{f}}{2} \end{cases} \ldots\ldots eq.(9)$$

$$\begin{cases} \Delta\mu_{Zr} = \mu_{Zr} - \mu_{Zr}^{*} < 0 \\ \Delta\mu_{Zr} > {}^{1}/_{2}\left(E_{ZrC}^{f} + E_{ZrO_2}^{f}\right) \end{cases} \ldots\ldots eq.(10)$$

$E_{ZrO_2}^{f}$ is the formation energy of ZrO_2, calculated as -4.98 eV and E_{ZrC}^{f} is the formation energy of ZrC. Thus, the chemical potential ranges are $-5.78\ eV < \Delta\mu_{Zr} < 0$ and $-4.98 < \Delta\mu_O < 0$. A plot of $\gamma_{int}^{i/j}$ against $\Delta\mu_O$ and $\Delta\mu_{Zr}$ is obtained and the stabilities of the different interface models are analyzed. The references used to define these limits are the optimized solids without any constraint or stress.

3. Results and Discussion

3.1 XPS, ToF-SIMS and TEM-ED Experiments

The XPS analysis of $ZrC_{0.96}O_{0.04}$, summarized in Table 2, reveals that the surface is contaminated by adventitious carbon (C 1s Binding Energy, BE = 284.5 eV) and Zr oxide (Zr 3d BE = 182.3 eV).

Table 2. XPS characterization of $ZrC_{0.96}O_{0.04}$

Element	Binding energy (eV)	FWHM (eV)	Proportion (%)	Atomic concentration (%)
Zr $3d_{5/2}$ (ZrC)	178.8	1.1	57	25.3
Zr $3d_{5/2}$ (ZrO_2)	182.3	1.3	43	
O 1s (ZrO_2)	530.0	1.7	46	45.2
O 1s	531.7	1.7	54	
C 1s (ZrC)	281.1	0.9	44	26.9
C 1s	284.5	1.6	56	
S 2p (elemental)	162.1	2.1	37	2.6
S 2p (sulfates)	168.9	2.1	64	

It clearly evidences the presence of two different chemical environments for zirconium with the observation of two doublets in the Zr 3d spectral region that are attributed to ZrC (Zr $3d_{5/2}$ BE = 178.8 eV) [48,49] and ZrO_2 (Zr $3d_{5/2}$ BE = 182.3 eV) (Figures 4 and 5).

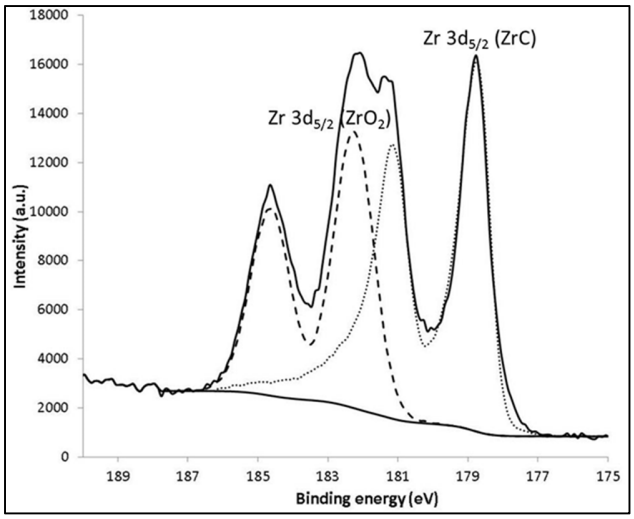

Figure 4. Decomposition of Zr 3d XPS spectrum for $ZrC_{0.96}O_{0.04}$ using line shapes defined from ZrO_2 and ZrC phases

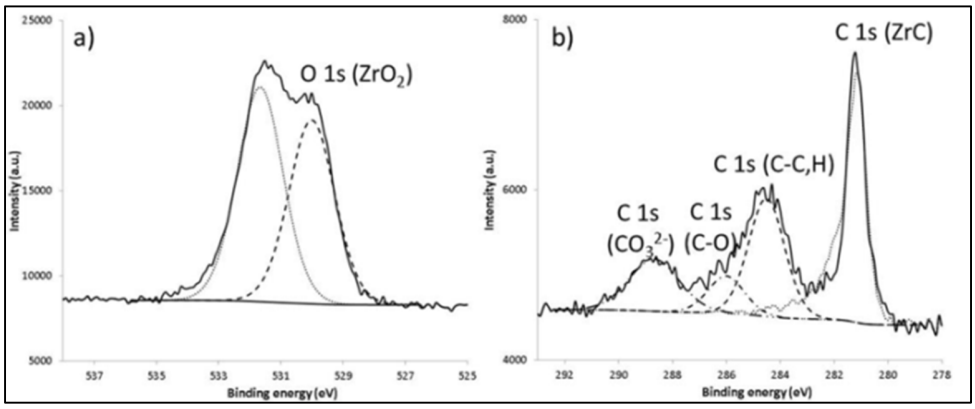

Figure 5. O 1s (a) and C 1s (b) XPS spectra for $ZrC_{0.96}O_{0.04}$

The decomposition of Zr 3d spectrum is performed using line shapes derived from data [50] of bulk reference materials of ZrO_2 and ZrC. On the one hand, the methodology consists in exposing $ZrC_{0.96}O_{0.04}$ to oxygen at 500°C for 1 h in a dedicated cell coupled to the XPS spectrometer then transferred into the XPS analysis chamber avoiding contamination. The oxidative treatment leads to the complete oxidation of the material into ZrO_2 (atomic Zr/O ratio of 0.5). On the other hand, the initial $ZrC_{0.96}O_{0.04}$ material was pressed into a pellet to operate an Ar^+ depth profile (2 keV, 3 mm x 3 mm). An extended (30 min) ion depth profile leads to the disappearance of the ZrO_2 contribution in Zr 3d region and to the appearance of asymmetric Zr 3d and C 1s photopeaks, characteristic of the metallic character of ZrC (atomic Zr/C ratio of 1.2). The atomic Zr/C ratio, calculated from the Zr 3d (ZrC) and C 1s (ZrC) contributions, is equal to 1.1, in good agreement with the expected ratio in ZrC phase. Furthermore, the atomic Zr/O ratio, calculated from the Zr 3d (ZrO_2) and O 1s (ZrO_2) components, is of 0.6, close to the theoretical Zr/O ratio in ZrO_2 phase.

In addition, the ZrO_2 layer thickness (d_{ZrO_2}) can be evaluated using a homogenous and continuous layer model [51] of intensity attenuation in which the $\frac{I_{Zr\,3d\,(ZrO_2)}}{I_{Zr\,3d\,(ZrC)}}$ ratio is expressed as:

$$\frac{I_{Zr\,3d\,(ZrO_2)}}{I_{Zr\,3d\,(ZrC)}} = \frac{I^{\infty}_{Zr\,3d\,(ZrO_2)}\,(1-\exp(-\frac{-\,d_{ZrO_2}}{\lambda_{Zr\,3d\,(\rightarrow ZrO_2)}}))}{I^{\infty}_{Zr\,3d\,(ZrC)}\,\exp(-\frac{-\,d_{ZrO_2}}{\lambda_{Zr\,3d\,(\rightarrow ZrC)}}))}$$

where $I_{Zr\,3d\,(ZrO_2)}$ and $I_{Zr\,3d\,(ZrC)}$ are the intensities of the two respective components of the XPS Zr 3d signal of $ZrC_{0.96}O_{0.04}$, $I^{\infty}_{Zr\,3d\,(ZrO_2)}$ and $I^{\infty}_{Zr\,3d\,(ZrC)}$ are the intensities of the XPS Zr 3d signal of ZrO_2 and ZrC reference samples (assuming a homogeneous material with infinite thickness), respectively, and $\lambda_{Zr\,3d\,(\rightarrow ZrO_2)}$ and $\lambda_{Zr\,3d\,(\rightarrow ZrC)}$ are the inelastic mean free paths of the electrons calculated from the TPP2M formula. [52] Their values are of 2.2 nm. Then the ZrO_2 layer thickness (d_{ZrO_2}) is estimated to 3.2 nm.

In the static ToF-SIMS analysis, isotopic patterns detected at ZrC surface in positive mode match with ZrO_2 reference. During the dynamic SIMS depth profiling, an initial lower energy profiling showed ZrO_2^- peaks when the sputtering starts, but the intensities of the ZrO_2^- and O^- peaks decrease with time. A similar pattern was observed at high energy sputtering (1kV) as shown in figure 6. Moreover, even though the dynamic SIMS depth profile experiment was conducted under vacuum, there was still a re-oxidation of the ZrC surface after some few minutes into the spectrometer.

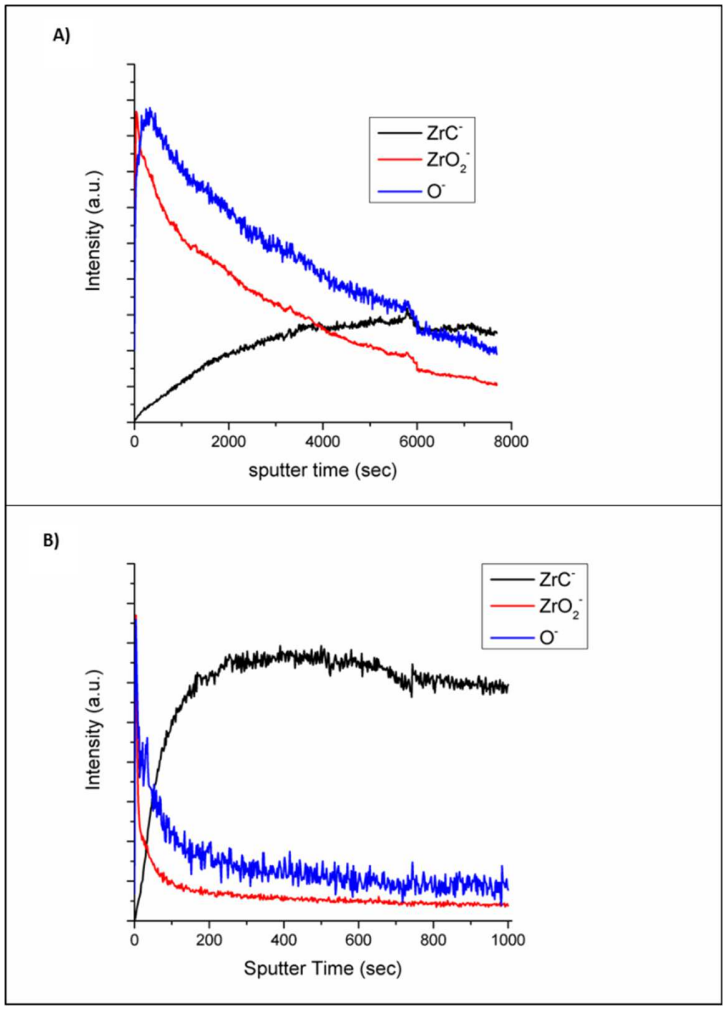

Figure 6. ToF-SIMS depth profiling with low energy (A) Cs^+ : 0.5kV – 30 nA – rastered over an area of 500µm x 500µm and high energy depth profiling (B) Cs^+: 1kV – 60 nA – rasterd over an area of 300µm

Even under vacuum ($1x10^{-8}$ mbar) there was a quick re-oxidation of ZrC after Cs^+ etching (Figure 7). Thus, the ZrC surfaces are highly reactive to oxygen as shown in several experimental and theoretical works [7-10,13,18]. Nevertheless, an attempted estimation of the oxide layer thickness can be done on the high energy ToF SIMS depth profile, in which the ZrO_2/ ZrC interface is defined (Figure 6B). In these experimental conditions, the sputter yield is assumed to be 1.38, allowing for a calculation of 7 nm for the oxide layer thickness, taking into account a density of 4.29 at./cm^3.

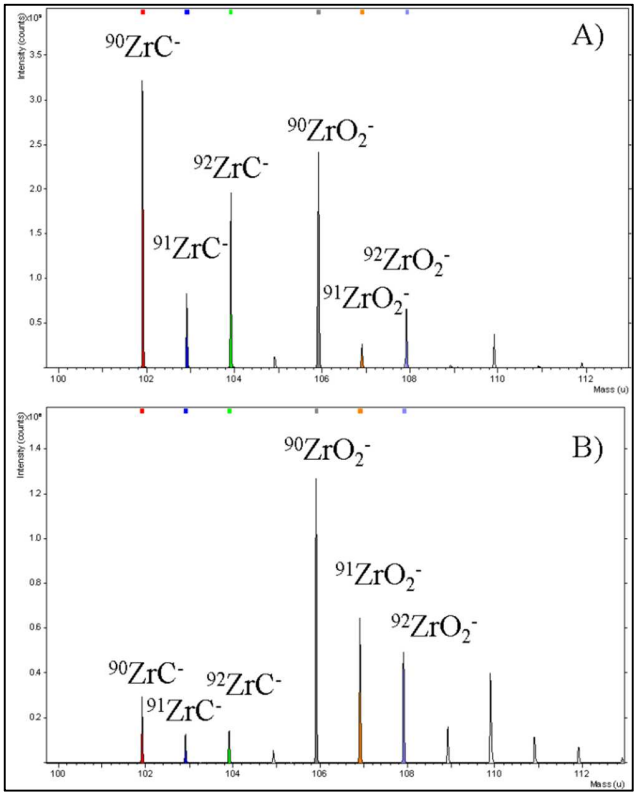

Figure 7. ToF-SIMS spectra in the m/z range (100-113). A) is a spectra acquired few seconds after a low energy depth profiling and B) is a spectra acquired about 5 minutes after low energy depth profiling

The TEM-ED experiment revealed the presence of a phase different from the bulk ZrC at the particle surface. EDX elemental analysis showed this phase to be zirconium oxide (Figure 8). This oxide layer thickness was estimated to be around 5 nm. This value is in correlation with the calculations carried out by surface analysis, 3 and 7 nm, by XPS and ToF SIMS depth profile, respectively.

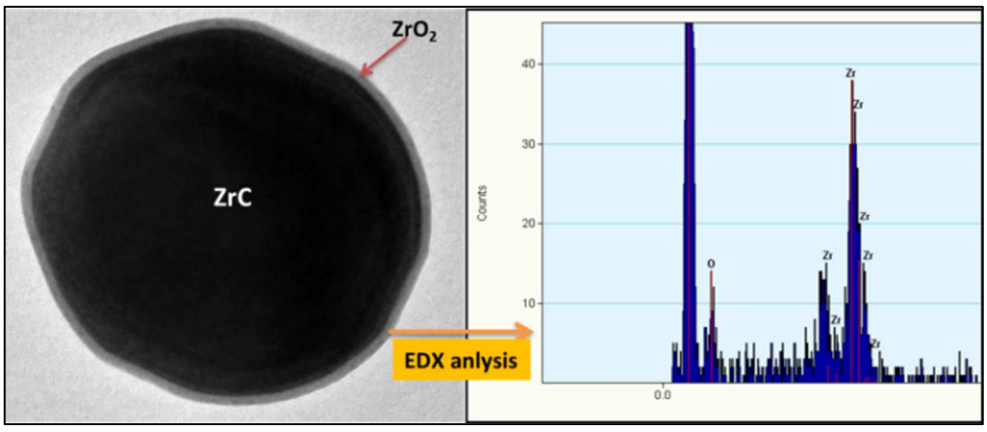

Figure 8. TEM and EDX identification of Zirconium Oxide on ZrC particles

According to high resolution imaging, orientations were clearly observed. This reflects that the oxide layer was crystalline. Two different areas were observed to show different crystal orientations (Figure 9A). Rings were obtained from the diffraction pattern obtained from the oxide layer and this confirmed the surface thin layer of oxide to be polycrystalline. A d_{hkl} indexation showed no possible correlation of the diffraction pattern with ZrC phase (Figure 9B). According to the lattice parameters calculated, there was no presence of monoclinic ZrO_2 but predominant amounts of cubic ZrO_2 and some traces of tetragonal ZrO_2.

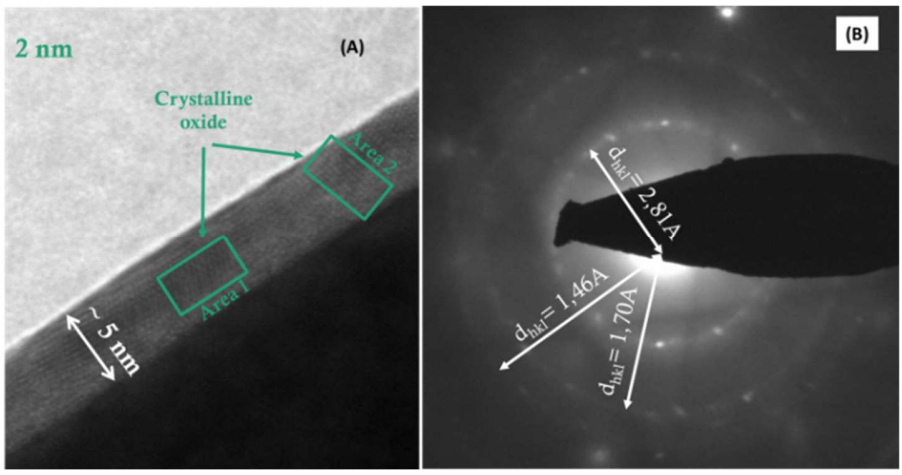

Figure 9. ED pattern and d_{hkl} indexation of Zirconium Oxide layer on ZrC particle surface

3.2 Finite Temperature MD

A brief discussion of the results obtained during the finite temperature MD simulations is provided here. At the highest temperature of 1000 K, there was a haphazard formation of ZrO_2 on the ZrC surface. Different coordinated O and Zr atoms were observed. Both four-fold and three-fold coordination types were detected for O atoms while five-fold and six-fold coordination was observed for Zr atoms. At the interface, all Zr atoms from ZrO_2 sat directly atop surface C atoms of ZrC, and O atoms from ZrO_2 formed mixed type of bonding at the interface. Some O atoms bonded directly on top surface Zr atoms of ZrC while some O atoms formed a three-fold bond between two surface Zr atoms and a C atom of ZrC, as previously observed in other calculations on the oxidation of ZrC(100) surface. [18] The under coordinated O and Zr atoms at this stage were typical of *m*-ZrO_2.

Upon quenching the structure at 500 K temperature, a more ordered structure was obtained. Eight-fold Zr and four-fold O atoms were observed in the ZrO_2 structure formed, typical of *t*- and *c*- ZrO_2 as confirmed by the experimental results above.

3.3 Bulk and surface properties of ZrC and ZrO_2

Details of the optimized lattice parameter, bulk modulus, and the pressure derivative of the bulk modulus for ZrC bulk phases were provided elsewhere. [18] Here, we consider optimized parameters for all three phases of ZrO_2. Thus, all characteristic bulk parameters needed to define all three ZrO_2 phases were well reproduced. Details on the lattice and bulk parameters are found in supporting information S.1. A summary of the bulk lattice parameters for ZrO_2 is provided in table S.1 (see supporting information).

The calculated surface energies for different layers of ZrC and all phases of ZrO_2 are summarized in table 3.

Table 3. Calculated surface energies eV/Å^2 for different layers of ZrC (001), *c*-, *t*- and *m*-ZrO_2 (001) surfaces

Number of Layers	ZrC (001)		*c*-ZrO_2(001)		*t*-ZrO_2(001)		*m*-ZrO_2(001)	
	unrelaxed	relaxed	unrelaxed	relaxed	unrelaxed	relaxed	unrelaxed	re-laxed
1 layer	0.135	0.135	0.229	0.144	0.231	0.205	0.257	0.069
2 layers	0.111	0.098	0.249	0.108	0.081	0.068	0.143	0.097
3 layers	0.108	0.098	0.252	0.109	0.205	0.175	0.149	0.090
4 layers	0.108	0.102	0.254	0.129	0.082	0.072	0.153	0.097
5 layers	0.107	0.100	0.255	0.130	0.203	0.193	0.158	0.102
6 layers	0.107	0.100	0.244	0.130	0.082	0.073	0.163	0.107

For ZrC (100) surface, the surface energy quickly converges from 2 layers upwards and computed surface energy is in very good agreement with previous calculations. [4] A plot of the surface energies at different layers is shown in figure 10. It is obvious from table 3 that the surface energy converges after 4 layers for both *c*-ZrO_2 (001) and *m*-ZrO_2 (001) surfaces. The unrelaxed surface energy of 0.252 eV/ Å^2(not shown in table 3) is in very good agreement with other values of 0.222 eV/ Å^2. [32] The surface energy of the relaxed structure is however 0.130 eV/ Å^2, about half of the unrelaxed structure. It is worth mentioning however that stoichiometric surfaces were only used with O terminations on both surfaces as this is found to be the predominantly exposed termination. [32] Relaxation in the c direction of the *c*-ZrO_2 surface resulted in distortion of the O atom positions along the *c*- axis.

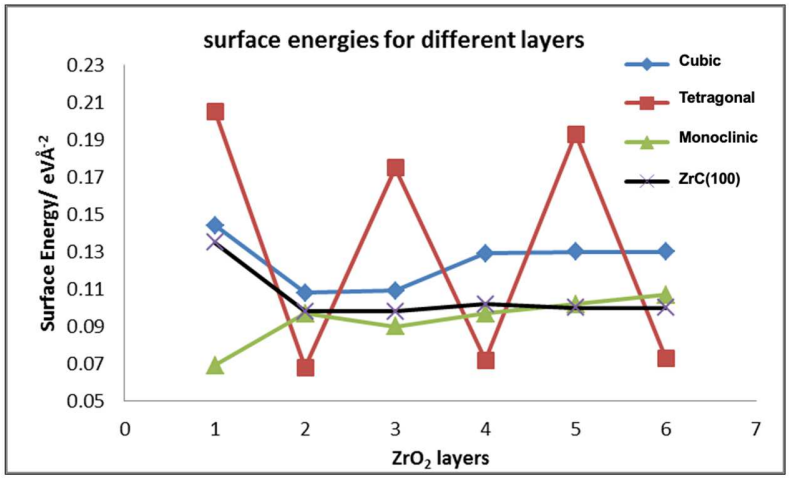

Figure 10. Calculated surface energies for different layers of ZrC (100) and *c*-, *t*-, *m*-ZrO_2 (001) surfaces

The unrelaxed surface energy of the monoclinic (001) is 0.150 eV/ Å^2 and is in excellent agreement with the LDA calculated value of 0.152[33] eV/ Å^2 and the GGA value of 0.123[53] eV/Å^2. Upon relaxation, the surface energy quickly converges to a value of 0.100 eV/ Å^2 after 4 layers. This is also in very good agreement with the LDA calculated value of 0.113[33] eV/ Å^2 and the GGA value of 0.084 eV/Å^2. [53]

An oscillating feature is observed for the surface energies for different layers of *t*-ZrO_2 as seen in figure 10. This feature has been noticed by other groups in their calculation of surface energy for different *t*-ZrO_2 layers. [35] This oscillating feature is a function of the odd/even nature of the number of layers used. Thus, even numbered layers give very stable surfaces while odd numbered layers give high energy surfaces. This same feature was observed by Christensen and Carter. [35] This effect may be related to the fact that odd-layered crystalline *t*-ZrO_2 (001) surface slabs have a $P\bar{4}m2$ symmetry while even-layered crystalline *t*-ZrO_2 (001) surface slabs have a *Pmmn* symmetry. [35] In another study, 4- layers and 12- layers of *t*-ZrO_2 (001) surface energies were calculated to be 0.069 eV/ Å^2 and 0.070 eV/ Å^2 respectively. [54] Thus the surface energy for these even-layered slabs is the same and lower than our calculated values for the odd- layered slabs. However, our calculated surface energy for the 4-layered slab is 0.072 eV/ Å^2 and in excellent agreement with the value calculated by Eichler and Kresse. [54]

3.4 Structure and cohesion at the Interface

3.4.1 Rigid Work of Adhesion

In this section results will be given for the rigid work of adhesion to provide understanding of the stability and mechanical behavior of the interface. As mentioned earlier, this work of adhesion is calculated by first obtaining the fully relaxed interface structure, then separating the two phases forming the interface and calculating their total energies without allowing them to relax. In this case, bulk properties of both ZrC and *c*-ZrO_2 are effectively cancelled out and the result depends purely on the interfacial properties. Table 4 provides a summary for the calculated rigid work of adhesion for the different interface models created. It is apparent from table 4 and figure

11(inset) that the Zr|OO|Zr|OO|Zr||oxidized-ZrC(100) interface has the strongest interaction at the interfacial region indicating this model as more stable with respect to cleavage. The calculated rigid work of adhesion (0.81 eV/Å^2) values are almost twice the values obtained for the other three interface structures. There is a convergence of the calculated values from 3 layers of *c*-ZrO_2 units.

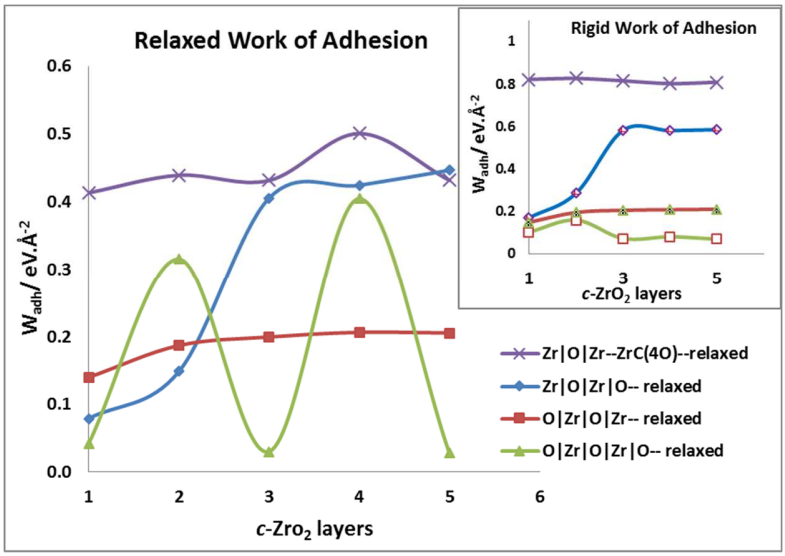

Figure 11. Calculated Work of Adhesion (W_{adh}) of different number of *c*-ZrO_2 (001) layers on ZrC(100) surface

3.4.2 Relaxed Work of Adhesion

The work of adhesion was calculated for the fully relaxed system in which the separated ZrC and *c*-ZrO_2 slabs are allowed to relax fully. In table 4, the relaxed work of adhesion calculated for the four different interface structures are provided. It becomes immediately evident that the Zr|OO|Zr|OO|Zr||oxidized-ZrC(100) model is the most stable interface. Thus, the relaxed work of adhesion confirms the most stable interface model obtained by the rigid work of adhesion. The relaxation process however results in a decrease of the work of adhesion as compared to the rigid model. The average difference between the rigid and relaxed work of adhesion is 0.40 eV/Å^2 for the Zr|OO|Zr|OO|Zr||oxidized-ZrC(100) system and this value is a result of interface slab relaxations. Thus after full relaxation, the resulting stable interface model is still Zr|OO|Zr|OO|Zr||oxidized-ZrC(100) and hence the relaxations do not affect the hierarchy of the works of separation.

Table 4. The rigid work of adhesion $\boldsymbol{W_{adh}^{rigid}}$ and the relaxed work of adhesion $\boldsymbol{W_{adh}^{relaxed}}$ for different layers of *c*-ZrO_2 (001) on ZrC (100). Interface model 1 is *Zr*|*OO*|*Zr*|OO||ZrC(100), model 2 is *O*|*Zr*|*OO*|*Zr*|O||ZrC(100), model 3 is *O*|*Zr*|*OO*|Zr||ZrC(100) and model 4 is *Zr*|*OO*|*Zr*|*OO*|Zr||oxidized ZrC(100)

c-ZrO_2 layers	Model 1	Model 2	Model 3	Model 4
	Rigid Work of Adhesion ($\boldsymbol{W_{adh}^{rigid}}$)/ eV.Å^{-2}			
1	0.170	0.103	0.149	0.822
2	0.286	0.160	0.196	0.827
3	0.583	0.073	0.206	0.816
4	0.581	0.081	0.209	0.803
5	0.586	0.070	0.211	0.809
	Relaxed Work of Adhesion ($\boldsymbol{W_{adh}^{relaxed}}$)/ eV.Å^{-2}			
1	0.079	0.042	0.140	0.413
2	0.148	0.315	0.187	0.439
3	0.406	0.030	0.199	0.432
4	0.425	0.405	0.206	0.501
5	0.447	0.028	0.205	0.432

Figure 11 shows oscillation of the relaxed work of adhesion for the O|Zr|OO|Zr|OO|Zr|O- model. Thus, even numbered layers of the *c*-ZrO_2(001) in this model forms a stronger interface than odd numbered *c*-ZrO_2(001) layers. It is worth noticing here that relaxation of the interface slab in the perpendicular direction to the interface results in transformation of the *c*-ZrO_2(001) phase into *t*-ZrO_2(001). As explained in section 3.3, the resulting *t*-ZrO_2(001) phase is like the *t*-ZrO_2(001) surface slab which terminates with O layers on both sides, and we observed this odd/even nature of the surface energies which is related to difference in symmetry of the odd/even slabs.

It is observed in table 4 that the W_{ad} value is the same for all layers of *c*-ZrO_2(001) added (for the stable interface model). This pattern is however not the same for the other three interface models. Thus, there is no systematic variation of the W_{ad} with the number of ZrO_2 layers and hence the chemistry of the ZrC(100)||*c*-ZrO_2(001) interface is local and defined by the ZrO_2 layer closest to the interface. In other words, long range interactions in ZrO_2 does not significantly contribute to the interfacial strength. The thicker ZrO_2 layer produces almost the same electrostatic image in ZrC as the thinner images and do not bond any stronger.

As defined in section 3.4.3, the interface tension can also be used to determine the strength of the bonds formed at the interface compared to the corresponding bond strengths in the respective bulk phases. In this case, the criteria are $0 < \gamma_{int} < \sigma_{ZrC} + \sigma_{c-ZrO_2}$ matching with weakly coupled interface and $\gamma_{int} < 0$ with strongly coupled interfaces. Using σ_{ZrC} = 0.100 eV/Å^2 and σ_{c-ZrO_2} = 0.129 eV/Å^2 asymptotic values from table 3, with relaxed W_{ad} = 0.455 eV/Å^2 for the most stable Zr|OO|Zr|OO|Zr||oxidized-ZrC(100) interface model, the calculated interface tension is γ_{int} = -0.226 eV/Å^2. Using value of σ_{t-ZrO_2} = 0.072 eV/Å^2 for even numbered layers and 0.175 eV/Å^2 for

odd numbered layers, we still obtain γ_{int} = -0.283 eV/Å^2 and -0.180 eV/Å^2 respectively. Thus, the negative sign of the interface tension shows that the interface bonds are stronger than the internal bonds in each ceramic phase.

3.4.3 Structure and properties at the Interface

In this section, we describe the structure and properties at the interface of the most stable model, Zr|OO|Zr|OO|Zr||oxidized-ZrC(100). In figure 12, the relaxed stable structures of the interface formed with 1, 2, 3, 4 and 5 layers of ZrO_2 are shown. During the relaxation process, the interfacial area is defined by the ZrC(100) substrate surface area and the pinned *c*-ZrO_2(001) overlayer is allowed to relax perpendicular to the interface. Figure 12 shows that, at all layers of ZrO_2 at the interface, there is the appearance of perpendicular relaxation of the O atoms of ZrO_2. Due to this oxygen displacement, the *c*-ZrO_2 phase is transformed into *t*-ZrO_2 one. It can be noticed the energy of the two phases is similar (ΔE= 0.054 eV/ ZrO_2 unit in table S.1).

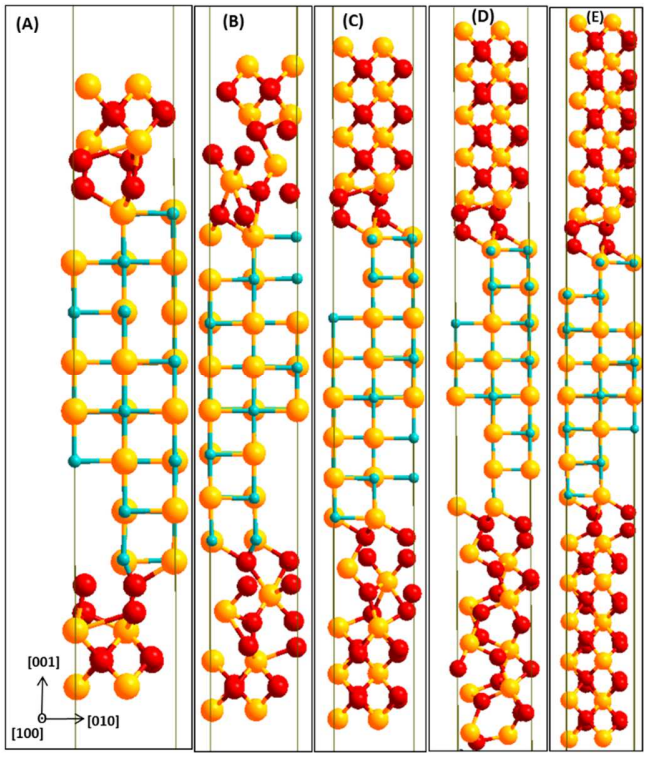

Figure 12. Lowest energy interface structures for 1 layer (A), 2 layers (B), 3 layers (C), 4 layers (D) and 5 layers (E) *c*-ZrO_2(001) for Zr|OO|Zr|OO|Zr||oxidized-ZrC(100) interface model. Yellow(Zr), light blue(C) and red(O)

The lowest energy 3-layer ZrO_2 interface slab was used to provide detailed description of the properties at the interface. During the relaxation process, the interface, the oxygen layer (4 atoms) is split into two. This splitting leads to inward relaxation (towards the ZrC side) of one of the Zr atoms (*c*-ZrO_2) and outward relaxation of the other Zr atom (*c*-ZrO_2). Even though the four O atoms forming the oxidized layer of the ZrC(100) surface are on

the same plane, upon forming the interface, two half of the O atoms move upwards to form strong bonds with the Zr atoms from *c*-ZrO_2. These O atoms form direct bonds with Zr atoms (ZrC side) in addition to the interfacial bonds formed. The same phenomenon in the opposite direction is maintained for the two O atoms (*c*-ZrO_2), which remains in their original planar positions. This explains the high work of adhesion calculated for this interface. There are twelve O – Zr bonds at the interface. The bond distances between the Zr (*c*-ZrO_2) atom closer to the interface and the interface O atoms (ZrC side) are 2.027 Å to 2.325 Å. The distances between the Zr (*c*-ZrO_2) atoms far from the interface and the interface O (ZrC) atoms are from 2.016 Å to 2.330 Å. At the region close to the interface (nearest first layer), there is the transformation of the *c*-ZrO_2 into *t*-ZrO_2 (101) with some three-fold and four-fold O atoms. Within this *t*-ZrO_2 (101) region, the three-fold O atoms have $d_{(O\text{-}Zr)\text{-}3f}$ bond distances of 2.027 Å, 2.051 Å and 2.189 Å while the four-fold O atoms have bond $d_{(O\text{-}Zr)\text{-}4f}$ of 2.161 Å, 2.271 Å, 2.232 Å and 2.799 Å.
After the first two layers of ZrO_2 at the interface, there is the transformation into *t*-ZrO_2(001). This can easily be seen by the tetragonal distortion observed in the last two oxygen layers away from the interface. Thus, two phases of *t*-ZrO_2 are observed forming the interface: *t*-ZrO_2(101) and *t*-ZrO_2(001). The phase at the interface region is *t*-ZrO_2(101) and the phase at the exposed surface of the interface slab is *t*-ZrO_2(001). These transformations are the results of compensating for the strain imposed on *c*-ZrO_2 as it is pinned onto the ZrC surface. The observed ZrO_2 phases corroborate the experimental results in the TEM-ED analysis. The d_{hkl} indexation revealed intense peaks for *t*-ZrO_2(101) phase. The transformation into *t*-ZrO_2 is necessary to alleviate part of the strain imposed on the *c*-ZrO_2 when forced into registry with the ZrC surface.

3.5 Thermodynamic Stability of Interface Models

Aside the use of the energetic parameters such as the work of adhesion and the interface tension to characterize the interface, the significance of a thermodynamic analysis of stability of the different interface models considered is nevertheless important. The predominant parameter used in assessing the interfacial stability is the interface grand potential, $\Omega_{int}^{i/j}$ which is the interface analogue of surface energy or surface grand potential for non-stoichiometric surfaces. This parameter considers the bulk ZrC and *c*-ZrO_2 as the reference states in forming the interface. It is worth mentioning that the bulk *c*-ZrO_2 reference is in a strained state to accommodate the substrate ZrC phase. Thus the *a* and *b* lattice parameters of *c*-ZrO_2 are strained to those of ZrC(100) and the c lattice is allowed to relax in the z-direction of the bulk phase. The same strained *c*-ZrO_2 phase is used as the reference in calculating the surface energy, $\gamma_{ZrO_2}^{surf}$ (equation 8) of the exposed facets in the interface slab.

According to equation 7, the interface grand potential $\gamma_{int}^{i/j}$ is calculated for different values of $\Delta\mu_O$ and $\Delta\mu_{Zr}$ and a plot from the data is shown in figure 13. In this plot, low values of $\Delta\mu_O$ correspond to oxygen poor environments and high values of $\Delta\mu_O$ match with oxygen rich environments with similar criteria for the Zr chemical potential. According to the 2D plot in figure 13, two different interface models are stable at different combinations of Zr and O chemical potentials. The Zr|OO|Zr|OO||ZrC(100) interface model is stable for a narrow region of the Zr and O

chemical potential combinations (oxygen poor and zirconium rich environments). However, in a wide combination of Zr and O chemical potentials, the Zr|OO|Zr|OO|Zr||oxidized-ZrC(100) interface model is the most stable, confirming the stability criterion established by both the work of adhesion and the interface tension. This can be explained by two factors. First in the Zr|OO|Zr|OO|Zr||oxidized-ZrC(100) model, there are more oxygen atoms at the interface than the other three models leading to the formation of more (12 Zr – O) bonds. In addition to this factor, in the Zr|OO|Zr|OO|Zr||oxidized-ZrC(100) model, the surface exposed to vacuum is Zr-terminated, which is less stable than the O-terminated facets in ZrO_2. This leads to subsequent subtraction of a higher surface energy term in equation 8 than the other two models.

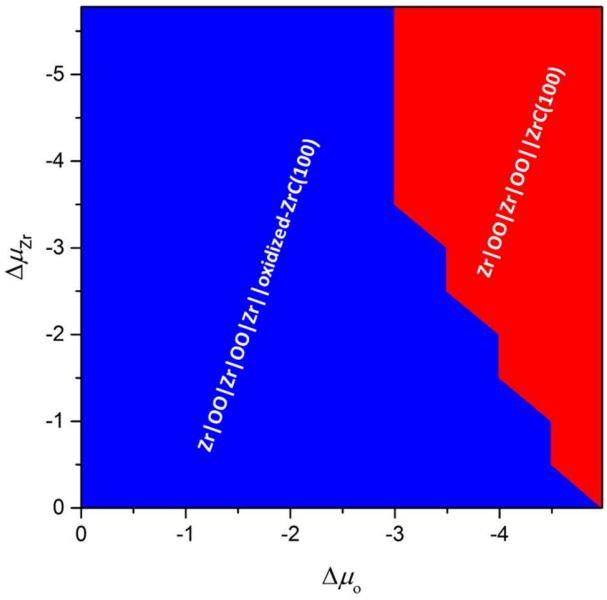

Figure 13. Stable interface models (lowest interface grand potential $\boldsymbol{\gamma_{int}^{i/j}}$) for different interface models as a function of $\Delta\boldsymbol{\mu_O}$ ***and*** $\Delta\boldsymbol{\mu_{Zr}}$.

3.6 Electronic properties at the interface

3.6.1 Density of States

In this section, we describe the electronic features at the interface region, more specifically, the density of states and charge analysis.

A description of the density of states (DOS) at the interface is first provided. A total spectrum was used, obtained by projecting the electronic states onto all atoms in the interface and separate surfaces as well as atomic spectra obtained by projecting the density of states onto individual atoms. Figure 14 shows the total DOS (TDOS) for the interface structure with 3 layers of ZrO_2.

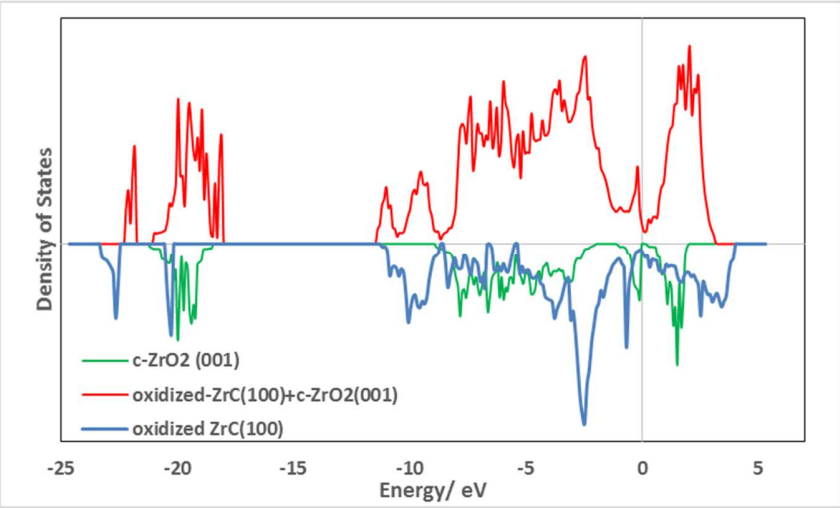

Figure 14. TDOS of interface model with 3 layers of *c*-ZrO_2(001) including the TDOS for the free oxidized ZrC(100) and *c*-ZrO_2(001) slabs.

Included are the TDOS for the corresponding surface slabs for oxidized ZrC and ZrO_2 used in constructing the interface model. Figure 14 shows that upon forming the interface, *c*-ZrO_2 fixed both in the valence band maximum and in the conduction band minimum. The main interfacial features around -5 eV are mainly due to the ZrO_2 states while those at -11 eV are due to the oxidized ZrC(100) states. In figure 15, the DOS are projected onto each atom at the interface and the corresponding atom in the surface slab. This helps in understanding the shift in the bands when the atoms form the interface structure.

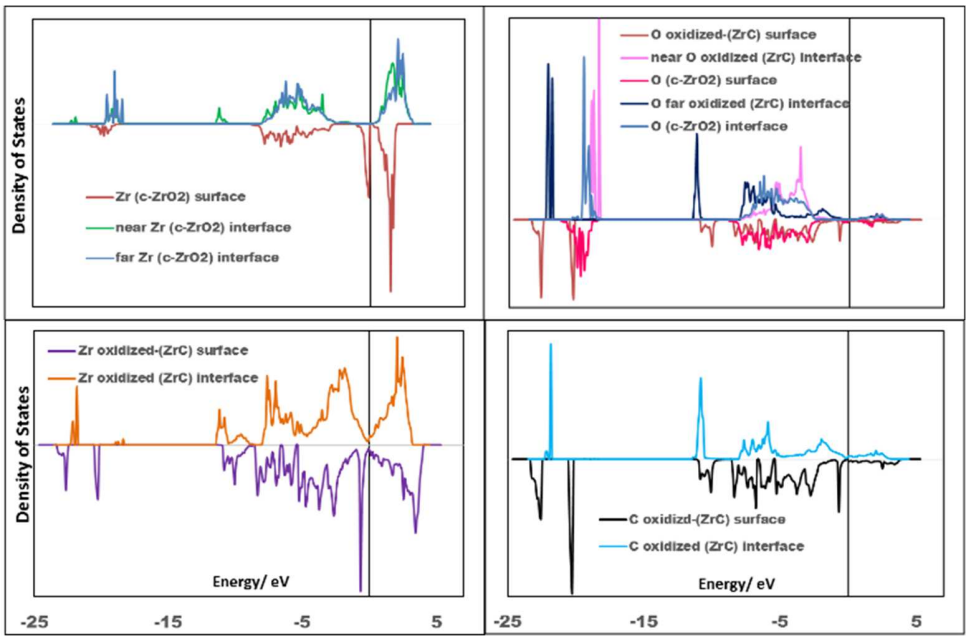

Figure 15. PDOS of each atom at the interface and in the corresponding surface slab. Spectra at the upper part of each plot are for atoms in the interface structure and those at the lower part are for the atoms in the corresponding surface slabs. Atoms labelled as near are closer to the interface plane than atoms labelled as far.

The O (oxidized ZrC) atom which sits closer to the ZrC side upon forming the interface, in an mmc site (three-fold bonding between two metal(Zr) and one C atom) shifts to higher energies in the core states and lower energies in the conduction band with the main interface features are at -11 eV and -22 eV (O s states are highly localized). This same localized band is found for the C and Zr (all oxidized ZrC side) at the interface at the same energy and shows the ionic nature of the C-O bond in the mmc configuration at the interface. In the conduction band, these O atoms however contribute significantly to the lower end in forming covalent bonds with Zr atoms (*c*-ZrO_2 side). The mmc O (oxidized ZrC) which is closer to the interface plane also shifts to higher energies with the main feature at -18 eV and contributes to the upper part of the valence band as it also forms covalent bonds with Zr (*c*-ZrO_2 side) at the interface. The localized conduction band in Zr (ZrO_2) is broadened upon forming the interface while the higher states at the Fermi level (highly unstable Zr-terminated *c*-ZrO_2 surface) are drastically reduced at the interface, stabilizing these atoms further. However, the Zr–O bond at the interface is highly covalent due to the diffuse nature of the Zr (*c*-ZrO_2) and O (oxidized ZrC) bands between -1 eV and -8 eV. To provide a good understanding of the evolution of the electronic structure of atoms moving from bulk to surface and then forming interface, figure 16 aligns the Projected Density of States (PDOS) for the atoms parallel to the interface plane. It shows the states for the atoms in both oxidized ZrC and *c*-ZrO_2 at the interface, in the bulk region of the slab and at the exposed surface in the vacuum area.

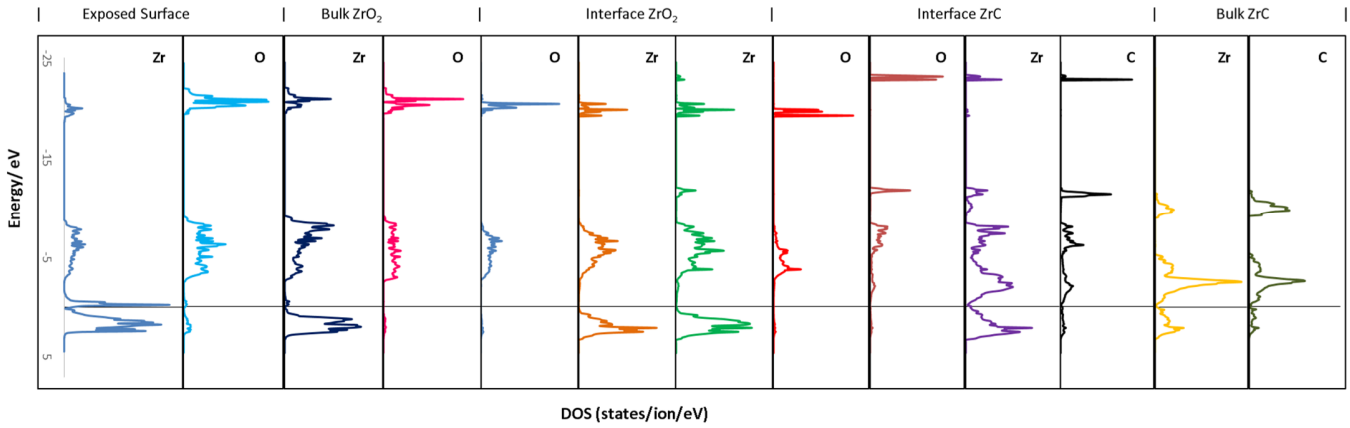

Figure 16. PDOS of atoms at the interface, in the bulk and the exposed surface of the three layer interface slab (Zr|OO|Zr|OO|Zr||oxidized-ZrC(100)). The states are aligned along the parallel plane to the interface with each region marked on the top layer. The Fermi level is aligned at the energy zero position.

The low energy area of the ZrO_2 bulk is made of much localized O 2s electrons and Zr 4d electrons at ~ -20 eV. However, the bulk ZrO_2 valence band is more covalent and made of O 2p and Zr 4d electrons and much more

diffuse than the low energy ionic bands at -20 eV. The conduction band for this bulk region is mainly Zr 4d. Moving to the exposed surface region, the valence band is highly diffuse, made of Zr 4d electrons and the conduction band is shifted to lower energies with Zr 4d states occupying the Fermi level. The high level of states at the Fermi level indicates a high reactivity of the exposed surface. The O 1s states at the lowest energy region are more diffuse than the bulk state, and the electrons are delocalized. In forming the interface, the O (oxidized ZrC side) adsorbed at the three-fold mmc site exhibits highly localized electrons shifted to higer energies at around -18 eV. The newly formed states at the interface are derived from the O 2p and O 1s (oxidized ZrC side) electrons mixing with Zr 4d (*c*-ZrO_2). This band (-11 eV) is very narrow indicating highly localized electrons in some of the Zr–O bonds formed at the interface. The Zr–O valence electrons are highly delocalized while the bands due to the far O (penultimate O atom to the interface on the *c*-ZrO_2 side) are less affected by the interface. At the ZrC end of the interface, the valence band consisting of mixed Zr d, p and s states shifts to higher energies towards the conduction band. The states arising from the mixing of the Zr (oxidized ZrC) and the far O (oxidized ZrC) at the interface are more diffuse and the electrons are delocalized. This stabilizes further the interface formed. Then, the C (oxidized ZrC) 2p states in the bulk become highly delocalized and shift to lower energies.

3.6.2. Charge Transfer Analysis

In this section, an analysis of charge transfer is provided during the formation of the interface. A somewhat intuitive idea of analyzing the charge transfer upon formation of the interface as described by Christensen and Carter[35] was used. Thus, the charge transfer values are arranged in a table in a form of spatial arrangement of the atoms from the surface to the respective layers of the phases forming the interface.

First the analysis of the charge distribution at the interface for the different layers was provided, starting from one to five layers of ZrO_2 in a spatial profile. Then, the charge redistribution in the three layer ZrO_2 interface slab (Zr|OO|Zr|OO|Zr||oxidized-ZrC(100)) from the interface to the bulk like ions, was analyzed.

According to table 5, there was a significant amount of charge transfer when the free surfaces came in contact to form an interface.

Table 5. Charge transfer analysis of Interfacial structure between oxidized ZrC(100) surface and different number of layers of *c*-ZrO_2(001) in the Zr|OO|Zr|OO|Zr||oxidized-ZrC(100) interface model. Values reported are net charges (electrons/atom) obtained with respect to the charges on the atom in the corresponding surface slabs that form the interface.

	Ion type		ZrO_2 layers on ZrC				
			1	2	3	4	5
ZrO_2 layer at Interface		O	-0.06	-0.03	-0.03	-0.03	-0.06
	Zr		-1.11	-1.04	-1.05	-1.05	-1.08
		Zr	-1.11	-1.07	-1.07	-1.09	-1.11
Interface Plane							
Oxidized ZrC layer at Interface	O		0.18	0.10	0.10	0.11	0.15
		O	0.10	0.08	0.11	0.10	0.10
	Zr		0.02	0.01	0.02	0.01	0.02
		C	1.03	1.03	1.03	1.01	1.03

The cations close to the interface provided most of the charge transfers. Moving from one layer of ZrO_2 upwards, there was essentially the same amount of charge transferred from Zr (*c*-ZrO_2) atoms to the interface atoms. The splitting of Zr atoms (*c*-ZrO_2) into near and far groups (with respect to the interface plane) did not result in any different in charge transferred by the two Zr groups. Nearly all the charge transferred from the interface cations were received by C atoms (oxidized ZrC side) resulting in an image charge phenomenon. This further explained why the interfacial strength was a local property confined to just the first and second ZrO_2 layers at the interface and did not depend on the number of layers added. The O atoms (oxidized ZrC side) received the same amount of charge from the *c*-ZrO_2 side corroborating the trend found using the mechanical property of the ideal work of adhesion (W_{ad}) in section 3.2.2.

4. Summary and Conclusions

The understanding of the structure and composition of ZrC-ZrO_2 interfaces is a key step to master the reactivity of the surface to generate hybrid core-shell systems, and to protect ZrC from oxidation at high temperatures. Thus, a combination of experiments, namely XPS, ToF-SIMS, TEM-ED and DFT calculations have been used to characterize and study the oxidation process on ZrC nano crystallites. According to the XPS analysis, two Zr $3d_{5/2}$ peaks were observed, and resolution showed the presence of two environments of Zr being ZrC and ZrO_2. The use of their XPS intensities showed ZrO_2 thickness on the ZrC surface to be 3.2 nm. ToF-SIMS analysis of the nano crystallites revealed ZrO_2- peaks and there was re-oxidation of the particles even with measurements under vacuum (1 x 10^{-8} mbar). Using TEM experiments a different phase as a shell around the ZrC particles was observed, and EDX analyses showed this phase to be ZrO_2. Further ED investigations estimated the oxide layer to be about 5 nm and two different crystal orientations were observed showing the polycrystalline nature of the particles. The ED analysis

revealed the presence of mainly cubic ZrO_2 with the presence of some tetragonal ZrO_2, mainly the (101) phase. Moreover, finite temperature molecular dynamics was used to grow ZrO_2 on the ZrC surface from Zr and O atoms and the formation of an ordered phase of cubic ZrO_2 on the ZrC (100) surface was observed. Furthermore, DFT was used to model the interface formed between ZrC and ZrO_2 phases and the preferred interface consisting of ZrO_2 terminating with Zr atoms at the interface side on an oxidized ZrC (100) surface, was highlighted. The main mechanical property used to characterize the interfacial strength was the ideal work of adhesion (W_{ad}). The calculated W_{ad} values showed that the interface strength remained quite constant, moving from one-layer ZrO_2 up to three layers ZrO_2 from which it converged. Thus, the interfacial strength depended on only the first ZrO_2 layer and not on subsequent layers. Thermodynamic analysis using the interface grand potential, $\Omega_{int}^{i/j}$ provided further evidence of a most stable interface formed. Further analysis on the electronic structure, using DOS and Bader charge analysis corroborated the local effect of the interface phenomenon. To conclude, these results constitute new important insights in the structure and composition of ZrC, that will undoubtedly have fallouts in the field of hybrid materials, and core-shell systems, obtained from non-oxide ceramics.

Acknowledgment

Numerical results presented in this paper were carried out using the regional computational cluster supported by Université Lille 1, CPER Nord-Pas-de-Calais/FEDER, France Grille, and CNRS. We highly appreciate and thank the technical staff of the CRI-Lille 1 center for their strong and helpful support.

The Chevreul Institute is thanked for its help in the development of this work through the ARCHI-CM project supported by the “Ministère de l’Enseignement Supérieur de la Recherche et de l’Innovation”, the region “Hauts-de-France”, the ERDF program of the European Union and the “Métropole Européenne de Lille”.The project is supported by Agence Nationale de la Recherche under Contract No. ANR-12-BS08-004-02 (CollZSiC: Elaboration de nanocomposites coeur/coquille ZrC/SiC).

Abbreviations

UPS, Ultraviolet Photoemission Spectroscopy; XPS, X-ray Photoemission Spectroscopy; ToF-SIMS, Time of Flight Secondary Ion Mass Spectrometry; TEM, Transmission Electron Microscopy; ED, Electron Diffraction; EDX, X-ray Diffraction Analysis.

References

(1) D. Gosset, M. Dollé, D. Simeone, G. Baldinozzi, L. Thomé, Structural Evolution of Zirconium Carbide under Ion Irradiation, J. Nucl. Mater. 373 (2008) 123-129. https://doi.org/10.1016/j.jnucmat.2007.05.034.

(2) D. Gosset, M. Dollé, D. Simeone, G. Baldinozzi, L. Thomé, Structural Behaviour of Nearly Stoichiometric ZrC under Ion Irradiation, Nucl. Instrum. Methods Phys. Res. Sect. B Beam Interact. Mater. At. 266 (2008) 2801–2805. https://doi.org/10.1016/j.nimb.2008.03.121.

(3) T. Das, S. Deb, A. Mookerjee, Study of Electronic Structure and Elastic Properties of Transition Metal and Actinide Carbides, Phys. B Condens. Matter 367 (2005) 6–18. https://doi.org/10.1016/j.physb.2005.05.041.

(4) E. Osei-Agyemang, J.-F. Paul, R. Lucas, S. Foucaud, S. Cristol, Stability, Equilibrium Morphology and Hydration of ZrC(111) and (110) Surfaces with H2O: A Combined Periodic DFT and Atomistic Thermodynamic Study, Phys. Chem. Chem. Phys. 33 (2015) 21401–21413. https://doi.org/10.1039/C5CP03031E.

(5) A. Arya, E. A. Carter, Structure, Bonding, and Adhesion at the ZrC(100)/Fe(110) Interface from First Principles, Surf. Sci., 560 (2004) 103–120. https://doi.org/ 10.1016/S0039-6028(04)00424-8.

(6) H. Li, L. Zhang, L. Cheng, Y. Wang, Oxidation Analysis of 2D C/ZrC–SiC Composites with Different Coating Structures in CH4 Combustion Gas Environment, Ceram. Int. 35 (2009) 2277–2282. https://doi.org/ 10.1016/j.ceramint.2008.12.002.

(7) T. Noda, M. Yamazaki, K. Ozawa, K. Edamoto, S. Otani, Oxygen Adsorption on a ZrC(111) Surface: Angle-Resolved Photoemission Study, Surf. Sci. 450 (2000) 27–33. https://doi.org/10.1016/S0039-6028(99)01235-2.

(8) A. Vojvodic, C. Ruberto, B. I. Lundqvist, Atomic and Molecular Adsorption on Transition-Metal Carbide (111) Surfaces from Density-Functional Theory: A Trend Study of Surface Electronic Factors, J. Phys. Condens. Matter Inst. Phys. J. 22 (2010) 375504. https://doi.org/10.1088/0953-8984/22/37/375504.

(9) T. Noda, T. Nakane, K. Ozawa, K. Edamoto, S. Tanaka, S. Otani, Photoemission Study of the Oxidation of ZrC(111), Solid State Commun. 107 (1998) 145–148. https://doi.org/10.1016/s0039-6028(99)01235-2.

(10) K. Ozawa, T. Yoshii, T. Noda, K. Edamoto, S. Tanaka, Coadsorption of Oxygen and Cesium on ZrC(111), Surf. Sci. 511 (2002) 421–434. https://doi.org/10.1016/S0039-6028(02)01552-2.

(11) S. Shimada, M. Yoshimatsu, M. Inagaki, S. Otani, Formation and Characterization of Carbon at the ZrC/ZrO2 Interface by Oxidation of ZrC Single Crystals, Carbon 36 (1998) 1125–1131. https://doi.org/10.1016/S0008-6223(98)00087-6.

(12) S. Shimada, M. Inagaki, M. Suzuki, Microstructural Observation of the ZrC/ZrO2 Interface Formed by Oxidation of ZrC, J. Mater. Res. 11 (1996) 2594–2597. https://doi.org/10.1557/JMR.1996.0326.

(13) E. Osei-Agyemang, J.-F. Paul, R. Lucas, S. Foucaud, S. Cristol, Oxidation and Equilibrium Morphology of Zirconium Carbide Low Index Surfaces Using DFT and Atomistic Thermodynamic Modeling, J. Phys. Chem. C 120 (2016) 8759–8771. https://doi.org/ 10.1021/acs.jpcc.6b01460.

(14) Kitaoka, H.; Ozawa, K.; Edamoto, K.; Otani, S. The Interaction of Water with Oxygen-Modified ZrC(100) Surfaces. Solid State Commun. 2001, 118 (1), 23–26. https://doi.org/ 10.1021/acs.jpcc.6b01460.

(15) K. Shin, O. Ken-ichi, E. Kazuyuki, O. Shigeki, Photoelectron Spectroscopy Study of the Oxidation of ZrC(100), Jpn. J. Appl. Phys. 39 (2000) 5217. https://doi.org/10.1143/JJAP.39.5217.

(16) F. Viñes, C. Sousa, F. Illas, P. Liu, J. A. Rodriguez, Density Functional Study of the Adsorption of Atomic Oxygen on the (001) Surface of Early Transition-Metal Carbides, J. Phys. Chem. C 111 (2007) 1307–1314. https://doi.org/10.1021/jp065126i.

(17) J. A. Rodriguez, P. Liu, J. Gomes, K. Nakamura, F. Viñes, C. Sousa, F. Illas, Interaction of Oxygen with ZrC(001) and VC(001): Photoemission and First-Principles Studies, Phys. Rev. B 72 (2005) 075427. https://doi.org/10.1103/PhysRevB.72.075427.

(18) E. Osei-Agyemang, J. F. Paul, R. Lucas, S. Foucaud, S. Cristol, Periodic DFT and Atomistic Thermodynamic Modeling of Reactivity of H2, O2, and H2O Molecules on Bare and Oxygen Modified ZrC (100) Surface, J. Phys. Chem. C 118 (2014) 12952–12961. https://doi.org/10.1021/jp503208n.

(19) F. Viñes, C. Sousa, F. Illas, P. Liu, J. A. Rodriguez, A Systematic Density Functional Study of Molecular Oxygen Adsorption and Dissociation on the (001) Surface of Group IV-VI Transition Metal Carbides, J. Phys. Chem. C 2007, 111 (45), 16982–16989. https://doi.org/10.1021/jp0754987.

(20) T. Shimada, K. Imamura, K. Edamoto, H. Orita, Electronic Structures of the Suboxide Films Formed on TiC(100) and ZrC(100) Surfaces: Density Functional Theory Studies, Surf. Sci. 603 (2009) 2340–2344. https://doi.org/10.1016/j-susc.2009.05.018.

(21) D. A. Shirley, High-Resolution X-Ray Photoemission Spectrum of the Valence Bands of Gold, Phys. Rev. B 5 (1972) 4709–4714. https://doi.org/10.1103/PhysRevB.5.4709.

(22) J. Hafner, Ab-Initio Simulations of Materials Using VASP: Density-Functional Theory and beyond, J. Comput. Chem. 29 (2008) 2044–2078. https://doi.org/10.1002/jcc.21057.

(23) N. D. Mermin, Thermal Properties of the Inhomogeneous Electron Gas, Phys. Rev. 137 (1965) A1441–A1443. https://doi.org/10.1103/PhysRev.137.A1441.

(24) G. Kresse, D. Joubert, From Ultrasoft Pseudopotentials to the Projector Augmented-Wave Method, Phys. Rev. B 59 (1999) 1758–1775. https://doi.org/10.1103/PhysRevB.59.1758.

(25) J. P. Perdew, K. Burke, M. Ernzerhof, Generalized Gradient Approximation Made Simple, Phys. Rev. Lett. 77 (1996) 3865–3868. https://doi.org/10.1103/PhysRevLett.77.3865.

(26) M. Methfessel, A. T. Paxton, High-Precision Sampling for Brillouin-Zone Integration in Metals, Phys. Rev. B (40) 1989, 3616–3621. https://doi.org/10.1103/PhysRevB.40.3616.

(27) H. J. Monkhorst, J. D. Pack, Special Points for Brillouin-Zone Integrations, Phys. Rev. B 13 (1976), 5188–5192. https://doi.org/10.1103/PhysRevB.13.5188.

(28) P. Haas, F. Tran, P. Blaha, Calculation of the Lattice Constant of Solids with Semilocal Functionals, Phys. Rev. B 79 (2009), 085104. https://doi.org/10.1103/PhysRevB.79.085104.

(29) P. Bouvier, G. Lucazeau, Raman Spectra and Vibrational Analysis of Nanometric Tetragonal Zirconia under High Pressure, J. Phys. Chem. Solids 61 (2000) 569–578. https://doi.org/10.1016/S0022-3697(99)00242-5.

(30) M. Yashima, T. Hirose, S. Katano, Y. Suzuki, M. Kakihana, M. Yoshimura, Structural Changes of ZrO2-CeO2 Solid Solutions around the Monoclinic-Tetragonal Phase Boundary, Phys. Rev. B 51 (1995) 8018–8025. https://doi.org/10.1103/physrevb.51.8018.

(31) L. Martin, G. Vallverdu, H. Martinez, F. L. Cras, I. Baraille, First Principles Calculations of Solid–solid Interfaces: An Application to Conversion Materials for Lithium-Ion Batteries, J. Mater. Chem. 22 (2012) 22063–22071. https://doi.org/10.1039/c2jm35078e.

(32) Y.-L. Yang, X.-L. Fan, C. Liu, R.-X. Ran, First Principles Study of Structural and Electronic Properties of Cubic Phase of ZrO2 and HfO2, Phys. B Condens. Matter 434 (2014) 7–13. https://doi.org/10.1016/J.PHYSB.2013.10.037.

(33) A. Christensen, E. A. Carter, First-Principles Study of the Surfaces of Zirconia, Phys. Rev. B 58 (1998) 8050–8064. https://doi.org/10.1103/PhysRevB.58.8050.

(34) L. M. Liu, S. Q. Wang, H. Q. Ye, First-Principles Study of Metal/nitride Polar Interfaces: Ti/TiN, Surf. Interface Anal. 35 (2003) 835-841. https://doi.org/10.1002/SIA.1613.

(35) A. Christensen, E. A. Carter, First-Principles Characterization of a Heteroceramic Interface: ZrO2(001) Deposited on an Alpha-Al2O3(1(1)over-bar02) Substrate, Phys. Rev. B Condens. Matter Mater. Phys. 62 (2000), 16968–16983. https://doi.org/10.1103/PhysRevB.62.16968.

(36) X.-G. Wang, J. R. Smith, Si/Cu Interface Structure and Adhesion, Phys. Rev. Lett. 95 (2005) 156102. https://doi.org/10.1143/PhysRevLett.95.156102.

(37) A. Hashibon, C. Elsässer, Y. Mishin, P. Gumbsch, First-Principles Study of Thermodynamical and Mechanical Stabilities of Thin Copper Film on Tantalum, Phys. Rev. B 76 (2007), 245434. https://doi.org/10.1103/PhysRevB.76.245434.

(38) A. Hashibon, C. Elsässer, Approaches to Atomistic Triple-Line Properties from First-Principles, Scr. Mater. 62 (2010) 939–944. https://doi.org/10.1016/j.scriptamat.2010.03.004.

(39) A.-L. Dalverny, J.-S. Filhol, M.-L. Doublet, Interface Electrochemistry in Conversion Materials for Li-Ion Batteries, J. Mater. Chem. 21 (2011), 10134–10142. https://doi.org/10.1039/C0JM04202A.

(40) O. I. Malyi, Z. Chen, G. G. Shu, P. Wu, Effect of Sulfur Impurity on the Stability of Cubic Zirconia and Its Interfaces with Metals, J. Mater. Chem. 2011, 21 (33), 12363–12368. https://doi.org/10.1039/C1JM10908A.

(41) H. Dai, J. Du, L. Wang, C. Peng, X. Liu, First-Principle Study of the AlP/Si Interfacial Adhesion, Phys. B Condens. Matter 405 (2010) 573–578. https://doi.org/10.1016/j.physb.2009.09.068.

(42) K. Radican, N. Berdunov, G. Manai, I. V. Shvets, Epitaxial Molybdenum Oxide Grown on $\mathrm{Mo}(110)$: LEED, STM, and Density Functional Theory Calculations, Phys. Rev. B 2007, 75 (15), 155434. https://doi.org/10.1103/PhysRevB.75.155434.

(43) A. Hashibon, C. Elsässer, M. Rühle, Structure at Abrupt Copper–alumina Interfaces: An Ab Initio Study, Acta Mater. 53 (2005) 5323–5332. https://doi.org/10.1016/j.actamat.2005.07.036.

(44) M. W. Finnis, The Theory of Metal - Ceramic Interfaces, J. Phys. Condens. Matter 8 (1996), 5811. https://doi.org/10.1088/0953-8984/8/32/003

(45) M. Wuttig, X. Liu, Ultrathin Metal Films, Springer-Verlag, Berlin, 2004.

(46) L. B. Freund, S. Suresh, Thin Film Materials: Stress, Defect Formation and Surface Evolution, Cambridge University Press: Cambridge, England, 2003.

(47) A. Christensen, E. A. Carter, Adhesion of Ultrathin ZrO2(111) Films on Ni(111) from First Principles, J. Chem. Phys. 114 (2001) 5816–5831. https://doi.org/10.1063/1.1352079.

(48) D. Craciun, G. Socol, N. Stefan, G. Bourne, V. Craciun, Chemical Composition of ZrC Thin Films Grown by Pulsed Laser Deposition, Appl. Surf. Sci. 255 (2009) 5260–5263. https://doi.org/10.1016/j.apsusc.2008.08.097.

(49) R. Lucas, D. Pizon, E. Laborde, G. Trolliard, S. Foucaud, A. Maître, A Simple Route for Organic Covalent Grafting onto Zirconium Carbide Particles, Appl. Surf. Sci. 287 (2013) 411–414. https://doi.org/10.1016/j.apsusc.2013.09.170.

(50) D. Briggs, J. Grant, Surface Analysis by Auger and XPS, IM Publications and Surface Spectra Limited: UK, 2003.

(51) J. Grimblot, L'analyse de Surface Des Solides; Masson, 1995.

(52) S. Tanuma, C. J. Powell, R. D. Penn, Calculations of Electron Inelastic Mean Free Paths. V. Data for 14 Organic Compounds over the 50–2000 eV Range, Surf. Interface Anal. 21 (1994) 165–176. https://doi.org/10.1002/sia.740210302.

(53) W. Piskorz, J. Gryboś, F. Zasada, S. Cristol, J.-F.Paul, A. Adamski, Z. Sojka, Periodic DFT and Atomistic Thermodynamic Modeling of the Surface Hydration Equilibria and Morphology of Monoclinic ZrO2 Nanocrystals, J. Phys. Chem. C 115 (2011) 24274–24286. https://doi.org/10.1021/jp2086335.

(54) A. Eichler, G. Kresse, First-Principles Calculations for the Surface Termination of Pure and Yttria-Doped Zirconia Surfaces, Phys. Rev. B 69 (2004) 045402. https://doi.org/10.1103/PhysRevB.69.045402.

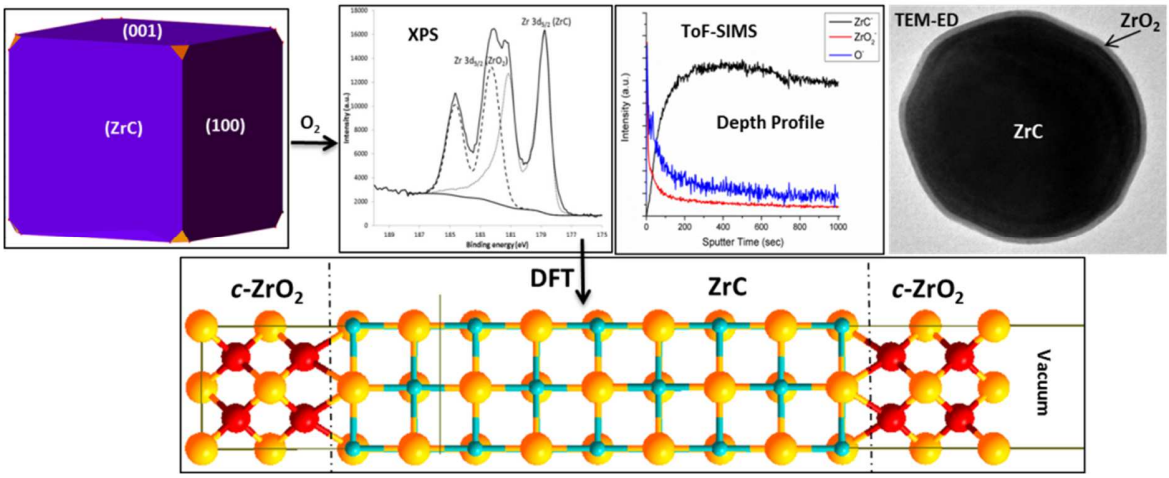
(001)
(ZrC)
(100)
O2
XPS
Zr 3d5/2 (ZrC)
Zr 3d5/2 (ZrO2)
Intensity (a.u.)
Binding energy (eV)
ToF-SIMS
ZrC
ZrO2
O
Depth Profile
Intensity (a. u.)
Sputter Time (sec)
TEM-ED
ZrO2
ZrC
DFT
c-ZrO2
ZrC
c-ZrO2
Vacuum
